frontiers | Frontiers in Energy Research

TYPE Original Research
PUBLISHED 21 January 2025
DOI 10.3389/fenrg.2024.1468496

OPEN ACCESS

EDITED BY
Shabana Urooj,
Princess Nourah bint Abdulrahman University, Saudi Arabia

REVIEWED BY
Mohammad Amir,
Indian Institutes of Technology (IIT), India
Omveer Singh,
Gautam Buddha University, India

*CORRESPONDENCE
Baheej Alghamdi,
baaalgamdi@kau.edu.sa

RECEIVED 22 July 2024
ACCEPTED 23 December 2024
PUBLISHED 21 January 2025

CITATION
Alghamdi B (2025) Distributed consensus-based voltage and frequency control for isolated microgrids with fault-induced delayed voltage recovery mitigation.
Front. Energy Res. 12:1468496.
doi: 10.3389/fenrg.2024.1468496

Distributed consensus-based voltage and frequency control for isolated microgrids with fault-induced delayed voltage recovery mitigation

Baheej Alghamdi[1,2]*

[1]Smart Grids Research Group, Center of Research Excellence in Renewable Energy and Power Systems, King Abdulaziz University, Jeddah, Saudi Arabia, [2]Department of Electrical and Computer Engineering, King Abdulaziz University, Jeddah, Saudi Arabia

This paper presents a distributed consensus-based voltage and frequency control (VFC) strategy for isolated microgrids with distributed energy resources (DERs) and induction motor loads. The proposed controller coordinates the DERs to regulate microgrid frequency and voltage while mitigating fault-induced delayed voltage recovery (FIDVR), a phenomenon where system voltage remains depressed for several seconds after fault clearance due to induction motor stalling. The VFC loop adjusts DER voltage setpoints based on frequency deviation and voltage level to regulate voltage and mitigate FIDVR events, while the active power control loop maintains frequency stability by coordinating active power sharing among DERs and compensating for the constant power load behavior of stalled induction motors. A proximity-based reactive power support prioritization and a distributed voltage estimator enhance the controller's response to FIDVR events. Coordination between the VFC and active power control loops is achieved through adaptive gain adjustment and a voltage recovery coordination term. Simulation results demonstrate the effectiveness of the proposed controller in maintaining microgrid stability, ensuring fast voltage recovery, and providing robust performance under various operating conditions, including communication delays and different fault durations.

KEYWORDS

distributed consensus control, voltage and frequency control, isolated microgrids, DERs, FIDVR, active power control, reactive power sharing

1 Introduction

Microgrids are gaining popularity as alternatives to traditional centralized power systems, addressing environmental and economic concerns. These local networks of distributed energy resources (DERs) and loads generate power to meet local demand, but the complex mix of energy sources and technologies presents challenges for operators and planners (Olivares et al., 2014). The intermittent behavior of DERs often leads to rapid frequency excursions during disturbances, especially when the microgrid is isolated. Thus, coordinated frequency control through distributed techniques is crucial for ensuring microgrid stability (Bidram, 2017).

Numerous studies have explored distributed and decentralized control techniques for frequency control in microgrids. Some focus on voltage

regulation-based frequency control, while others investigate specific aspects of microgrid dynamics or applications. This paper presents an enhanced operational control scheme that effectively manages isolated microgrids, addressing both frequency regulation and fault-induced delayed voltage recovery (FIDVR). The literature review analyzes the advantages of this study compared to existing research.

Farrokhabadi et al. (2017) presents a frequency control mechanism for isolated microgrids based on voltage regulation, but it lacks co-optimization with active power sharing control and a precise mechanism to mitigate FIDVR events. Similarly, (Farrokhabadi et al., 2016) introduces a novel voltage-based controller for frequency control in inverter-based isolated microgrids, offering advantages such as decreased system dependency on energy storage and higher penetration of renewable energy. However, it does not manage intricate microgrid dynamics and disturbances. The study by Farrokhabadi et al. (2021) explores the use of optimal voltage-based frequency control in islanded microgrids and demonstrates the robustness of the proposed VFC controller. However, the study does not consider the issue of power-sharing among DERs or provide a dedicated voltage control mode specifically designed to handle fault-induced delayed voltage recovery (FIDVR) events. Furthermore, the impact of VFC on microgrid stability in the presence of induction motor loads is not investigated in these studies.

Recent advances in distributed control strategies have focused on finite-time and predefined-time convergence to enhance the dynamic performance of microgrids. In Xu et al. (2019), an optimal distributed control strategy is proposed for the coordination of multiple distributed generators in an islanded microgrid, employing a finite-time secondary frequency control approach to eliminate frequency deviation and maintain accurate active power sharing. However, the approach does not address FIDVR events or the coordination between voltage control and reactive power sharing during such disturbances.

Similarly, (Choi et al., 2022) presents a distributed finite-time event-triggered secondary frequency and voltage control for islanded AC microgrids, effectively performing frequency restoration and voltage regulation while sharing active and reactive power among distributed generators. The event-triggered communication reduces the communication burden, but the study does not consider the mitigation of FIDVR events or the impact of induction motor loads on voltage stability.

In Huang et al. (2023), a novel distributed fractional-order predefined-time sliding mode controller is proposed as a secondary controller for islanded AC microgrids. The controller ensures that frequency and estimated average voltage converge to reference values within a predefined time, enhancing dynamic performance. Nevertheless, the study does not address FIDVR mitigation or the coordination between voltage control and reactive power sharing in the presence of induction motor loads.

Other studies focus on specific aspects of microgrid problems, such as utilizing DER smart inverters and FACTS devices for FIDVR mitigation. In Wang and de León (2020), smart inverters with voltage ride-through and var injection capabilities are exploited for the mitigation of FIDVR in distribution systems, showing that DER penetration levels significantly affect mitigation success. However, the study is centered on distribution systems rather than isolated microgrids and does not propose a coordinated control strategy among DERs.

Paredes et al. (2023) proposes an approach to incorporate flexible AC transmission system (FACTS) devices, such as SVC and DSTATCOM, into microgrids as reactive power supply resources for improving dynamic voltage stability and mitigating FIDVR. While effective in enhancing voltage stability, the solution relies on additional hardware infrastructure and does not leverage the existing DER capabilities for coordinated voltage and frequency control.

A model-free voltage control approach is presented in Park and Olama (2021) to mitigate motor stalling and FIDVR in smart grids, utilizing an intelligent PID controller without requiring complex dynamic models. This method simplifies implementation and reduces computational costs but does not consider the coordination among multiple DERs in a microgrid or address active power sharing and frequency regulation.

In Mohiuddin and Qi (2022), an optimal distributed voltage control for grid-forming inverters in islanded AC microgrids is proposed, formulating an optimization problem that balances voltage regulation and reactive power sharing. While the approach addresses coordinated voltage control and reactive power sharing, it does not specifically target FIDVR events or consider the impact of induction motor loads on microgrid stability.

Other studies focus on specific aspects of microgrid problems. Nayeripour et al. (2018) explores the challenge of protecting load buses serving three-phase induction motors using dynamic state estimation, but does not consider frequency regulation and FIDVR aspects. Benali et al. (2018) investigates the impact of induction motor load on the dynamic voltage stability of an isolated microgrid during faults and proposes a reactive power support control strategy using photovoltaic systems to mitigate dynamic voltage instability. Hossain et al. (2019) examines the starting capability of diesel generators and battery energy storage systems (BESS) in islanded microgrids with induction motors, proposing a Starting Capability Index (SCI) to assess the system's starting capability and improve dynamic performance, but does not address broader frequency regulation and FIDVR management capabilities.

Ling et al. (2021) presents a transient stability analysis of an induction motor-load system considering stator flux dynamics, while (Gu et al., 2022) investigates the transient stability of an induction motor-load system under voltage sag conditions, proposing a new method to analyze the system's transient stability. However, these studies do not provide a holistic and adaptive control strategy for managing intricate microgrid dynamics and disturbances in the context of frequency regulation and FIDVR scenarios.

Alghamdi (2022b) presents a fuzzy-logic-based voltage frequency control and adaptive inertia controller for improving the frequency response of a virtual synchronous generator (VSG) in an isolated microgrid system, but lacks seamless transition between control modes and a specialized voltage control mode for FIDVR events. Alghamdi (2022a) proposes a hierarchical distributed consensus control method for frequency regulation in isolated microgrids using voltage frequency control and active power regulation, but does not address FIDVR events or consider the impact of induction motor loads on microgrid stability.

The proposed distributed consensus-based voltage and frequency control (VFC) strategy offers significant advantages over existing VFC techniques. It addresses several gaps in the current literature and provides innovative solutions to enhance microgrid stability and resilience. Based on the reviewed literature, several limitations in existing microgrid control strategies can be identified:

1. Limited consideration of FIDVR events in VFC schemes.
2. Lack of coordination between VFC and active power control in distributed control architectures.
3. Insufficient attention to the impact of communication delays on distributed control performance.
4. Absence of adaptive control mechanisms to handle varying fault durations.

This paper addresses these gaps through the following key contributions:

1. A novel distributed consensus-based VFC strategy that effectively handles FIDVR events in isolated microgrids with induction motor loads. This strategy incorporates a specialized voltage control mode that addresses FIDVR events, introducing a proximity-based reactive power support prioritization and a distributed voltage estimator. This enhances the controller's response to FIDVR events and provides an accurate representation of the microgrid voltage profile, ensuring faster recovery times and improved voltage stability.
2. An adaptive gain adjustment mechanism in the active power control loop to maintain frequency stability and compensate for the constant power load behavior of stalled induction motors during FIDVR events. The proposed controller achieves effective coordination between the VFC and active power control through this mechanism and the inclusion of a voltage recovery coordination term in the active power setpoint calculation. This enables the active power control loop to provide a fast and robust response to frequency deviations caused by the constant power load behavior of stalled induction motors during FIDVR events, maintaining frequency stability while the VFC focuses on voltage recovery.
3. A comprehensive analysis of the proposed controller's performance under various communication delay scenarios, demonstrating its robustness in realistic microgrid applications.
4. An in-depth investigation of the controller's effectiveness in handling different fault durations, showcasing its adaptability to various disturbance conditions.

The remainder of this paper is organized as follows: Section 2 discusses the modeling of microgrid components, including static and dynamic loads, with a focus on the behavior of induction motor loads during FIDVR events. Section 3 introduces the proposed distributed consensus-based VFC strategy, detailing the voltage control loop, active power control loop, proximity-based reactive power support prioritization, and adaptive gain adjustment mechanism. Section 4 presents the simulation results and discussion, demonstrating the effectiveness of the proposed controller in maintaining microgrid stability, ensuring fast voltage recovery, and providing robust performance under various operating conditions. This section also investigates the impact of fault duration and communication delays on the controller's performance. Finally, Section 5 summarizes the main conclusions and highlights the significance of the proposed distributed consensus-based VFC strategy in enhancing the stability and resilience of isolated microgrids with induction motor loads.

2 Modeling and frequency regulation in microgrid architectures

Isolated microgrids face challenges in maintaining stable voltage and frequency due to the intermittent nature of renewable energy sources (RESs) and potential supply-demand imbalances. This paper focuses on developing a distributed consensus-based VFC strategy that operates at the primary and secondary control levels to ensure stable microgrid operation and mitigate fault-induced delayed voltage recovery (FIDVR) events.

The microgrid under study consists of diesel generators, battery energy storage systems (BESS), wind turbines, and dynamic loads such as induction motors. The diesel generators and BESS are modeled as grid-forming units, while the wind turbines are modeled as grid-following units. The induction motor loads are represented using a full-order wound rotor induction machine model to capture their dynamic behavior and potential for causing FIDVR events.

The proposed VFC strategy coordinates the control actions of the DERs to maintain stable voltage and frequency profiles, even in the presence of disturbances. By leveraging a distributed consensus approach, the VFC strategy enables efficient information exchange among the DERs and facilitates a coordinated response to mitigate FIDVR events and ensure reliable microgrid operation.

2.1 Static load modeling

In this study, the microgrid includes static loads that are modeled using an exponential voltage-dependent load model. This model captures the relationship between load demand and system voltage, as described by Equations 1, 2. Alghamdi and Cañizares (2021):

$$P_{L_l} = K_{LP_l} V_L^{\alpha_{pl}} \qquad \forall l \tag{1}$$

$$Q_{L_l} = K_{LQ_l} V_L^{\alpha_{ql}} \qquad \forall l \tag{2}$$

In these equations, P_{L_l} and Q_{L_l} represent the active and reactive power demand of load l, respectively, while V_L denotes the load voltage magnitude. The parameters K_{LP_l} and K_{LQ_l} are scaling factors specific to load l, and α_{pl} and α_{ql} are voltage exponents that define the load type characteristics.

The exponents α_{pl} and α_{ql} determine the sensitivity of the load to voltage changes. Common values represent different types of loads (e.g., constant power, constant current, constant impedance).

The voltage-dependent behavior of these static loads affects the power balance in the microgrid. As the system voltage decreases, the power consumption of these loads also decreases, and *vice versa*. This characteristic has implications for frequency regulation, as changes in voltage can influence the system's frequency through the load demand.

2.2 Induction motor loads and FIDVR

Induction motor loads constitute a significant portion of the load in microgrids and are a primary cause of fault-induced delayed voltage recovery (FIDVR) events due to their stalling behavior during voltage sags (Stefopoulos and Meliopoulos, 2006). In order to accurately study the impact of induction motor loads on FIDVR in microgrids, this paper utilizes a full-order wound rotor induction machine model provided by the PSCAD simulation software PSC (Wound rotor induction machine, 2023).

2.2.1 Dynamic model of the induction motor

The full-order wound rotor induction machine model represents the detailed electrical and mechanical dynamics of the induction motor, accounting for both the stator and rotor circuits as well as the mechanical dynamics of the rotor. The model is based on the following equations in the synchronous reference frame (Krause et al., 2013; Chapman, 2011).

2.2.1.1 Stator voltage equations

The q-axis and d-axis stator voltage dynamics are given by Equations 3 and 4, respectively.

$$\frac{d\psi_{qs}}{dt} = \omega_b\left(v_{qs} - R_s i_{qs} - \omega\psi_{ds}\right) \tag{3}$$

$$\frac{d\psi_{ds}}{dt} = \omega_b\left(v_{ds} - R_s i_{ds} + \omega\psi_{qs}\right) \tag{4}$$

2.2.1.2 Rotor voltage equations

Likewise, the q-axis and d-axis rotor voltage dynamics are formulated in Equations 5 and 6.

$$\frac{d\psi_{qr}}{dt} = \omega_b\left(v_{qr} - R_r i_{qr} - (\omega - \omega_r)\psi_{dr}\right) \tag{5}$$

$$\frac{d\psi_{dr}}{dt} = \omega_b\left(v_{dr} - R_r i_{dr} + (\omega - \omega_r)\psi_{qr}\right) \tag{6}$$

2.2.1.3 Flux Linkage equations

The flux linkage relationships are shown in Equations 7, 8, 9, and 10, capturing stator–rotor coupling.

$$\psi_{qs} = L_s i_{qs} + L_m i_{qr} \tag{7}$$

$$\psi_{ds} = L_s i_{ds} + L_m i_{dr} \tag{8}$$

$$\psi_{qr} = L_r i_{qr} + L_m i_{qs} \tag{9}$$

$$\psi_{dr} = L_r i_{dr} + L_m i_{ds} \tag{10}$$

2.2.1.4 Mechanical Equation

Equation 11 governs the mechanical dynamics of the rotor speed (ω_r) based on the torque imbalance.

$$\frac{d\omega_r}{dt} = \frac{1}{2H}\left(T_e - T_m\right) \tag{11}$$

TABLE 1 List of variables and parameters.

Symbol	Description
$\psi_{qs}, \psi_{ds}, \psi_{qr}, \psi_{dr}$	q-axis and d-axis stator and rotor flux linkages
$i_{qs}, i_{ds}, i_{qr}, i_{dr}$	q-axis and d-axis stator and rotor currents
$v_{qs}, v_{ds}, v_{qr}, v_{dr}$	q-axis and d-axis stator and rotor voltages
R_s, R_r	Stator and rotor resistances
L_s, L_r, L_m	Stator, rotor, and mutual inductances
ω	Synchronous speed
ω_r	Rotor speed
ω_b	Base electrical angular velocity
H	Inertia constant
T_e	Electromagnetic torque
T_m	Mechanical torque (load torque)
p	Number of pole pairs

2.2.1.5 Electromagnetic torque

The electromagnetic torque (T_e) is computed as shown in Equation 12, relating stator flux linkages and currents.

$$T_e = \frac{3}{2}p\left(\psi_{qs} i_{ds} - \psi_{ds} i_{qs}\right) \tag{12}$$

The definitions of the variables and parameters used in the above equations are listed in Table 1.

2.2.2 Behavior during FIDVR events

During voltage sags caused by faults, the reduced terminal voltage leads to a significant drop in the electromagnetic torque T_e, causing the induction motor to decelerate. If the voltage sag persists, the motor may reach a point where it stalls, i.e., the rotor speed ω_r decreases substantially.

When the fault is cleared and voltage is restored, the stalled induction motor attempts to reaccelerate, drawing a large inrush current and a substantial amount of reactive power due to the low rotor speed and high slip. This excessive reactive power demand can prevent the system voltage from recovering quickly, resulting in FIDVR.

By modeling the induction motor using the detailed equations presented above, we can simulate its dynamic response during faults and voltage recovery, capturing the stalling behavior and its impact on the microgrid voltage profile.

2.2.3 Impact on microgrid stability

The stalling and reaccelerating behavior of induction motors during and after faults poses significant challenges for microgrid stability. The prolonged voltage depression and increased reactive power demand can lead to:

- Delayed voltage recovery, affecting other voltage-dependent loads.

- Frequency deviations due to sudden changes in active power consumption.
- Potential cascading effects impacting overall microgrid performance.

2.2.4 Need for advanced control strategies

Addressing the challenges posed by induction motor loads during FIDVR events necessitates the development of advanced control strategies that can:

- Provide effective voltage support to facilitate rapid voltage recovery.
- Mitigate the excessive reactive power demand from stalled induction motors.
- Maintain frequency stability despite abrupt changes in load behavior.

These control strategies are critical for ensuring the reliable operation of isolated microgrids with significant induction motor loads. In the following sections, we will introduce and discuss the proposed distributed consensus-based voltage and frequency control strategy designed to tackle these challenges.

2.3 Diesel generators (diesel units)

Diesel generators play a crucial role in isolated microgrids, serving as reliable energy sources capable of providing continuous, uninterruptible power to meet the demand and facilitating frequency and voltage regulation. Diesel generators offer multiple advantages, such as their ability to start quickly, their dispatchability, and their capability of operating over a wide range of loading conditions. These characteristics render diesel generators particularly valuable in isolated microgrids, where other energy sources like renewable energy sources (RESs) can be intermittent and may exhibit unpredictable fluctuations (Vandoorn et al., 2011).

In isolated microgrids, diesel generators form an essential part of the primary control, responsible for maintaining the grid frequency and voltage profiles within acceptable limits. Since the diesel generators are coupled to the microgrid through their synchronous generators, their rotational speed is directly related to the system frequency. Consequently, diesel generators can adjust their mechanical input power to counteract variations in frequency due to mismatches between supply and demand, thus assisting in frequency control.

In isolated microgrids, Equation 13 describes the diesel generator's swing equation, relating rotor inertia (M_{DER}) and damping (D_{DER}) to the balance between mechanical input power (P_m) and electrical output power (P_{DER}). The swing equation is given by Bevrani (2017):

$$M_{DER}\frac{\mathrm{d}\omega}{\mathrm{d}t}+D_{DER}\Delta\omega=P_m-P_{DER} \tag{13}$$

where ω represents the rotor's angular velocity (speed), M_{DER} and D_{DER} are the diesel generator's inertia and damping coefficients respectively, P_m denotes the mechanical power input to the generator, and P_{DER} is the electrical output power.

The researchers referenced in Yeager and Willis (1993) have meticulously developed a dynamic model of a diesel generator that is tailored to perform optimally in time-domain simulations. This model is validated by its alignment with an actual field model. In the mentioned study, a comprehensive model is utilized, incorporating both the governor and exciter models. The gains in this model are aptly calibrated to the test system under examination.

Of particular significance is the choice of control mode for the governor model, which is set to Droop Mode as opposed to Isochronous Mode. Droop control is a widely used method for frequency regulation in power systems. It allows load sharing in multiple generator setups and maintains system stability under varying load conditions. The operation of the droop control governor can be quantitively represented by the droop control equation.

Consider, for instance, the following droop control equation as stated in Bevrani (2017):

$$K_{DER}\left(f_o-f_{MG}\right)=\left(P_{DER}-P_{DERo}\right) \tag{14}$$

Here, P_{DERo} signifies the nominal active power of the distributed energy resource (DER), f_o denotes the nominal system frequency, K_{DER} represents the droop coefficient, and f_{MG} is the observed operational frequency of the microgrid itself.

2.4 BESS model

In microgrids, battery energy storage systems (BESSs) play a crucial role in managing the rapid fluctuations in the output power of renewable energy sources, such as solar and wind generators (Olivares et al., 2014). BESSs are integrated into the microgrid through voltage source converters (VSCs), which enable them to respond quickly to changes in the system's frequency by delivering active power. This fast response is essential for maintaining the stability of the microgrid, as the dynamics of BESSs are significantly faster than those of conventional generators like diesel engines.

In this study, the BESS operates in a grid-feeding control mode, where it injects specified amounts of active and reactive power into the microgrid. The control strategy involves calculating the reference currents needed to achieve the desired power injection.

2.4.1 Mathematical model of the BESS operating in grid-feeding mode

The instantaneous active and reactive power injected by the BESS are calculated using Equation 15, which relies on the measured grid-side voltages and currents (Teodorescu, 2011; Yazdani, 2010):

$$\begin{aligned} p&=\frac{3}{2}\left(V_{gd}I_{gd}+V_{gq}I_{gq}\right)\\ q&=\frac{3}{2}\left(V_{gd}I_{gq}-V_{gq}I_{gd}\right)\end{aligned} \tag{15}$$

where:

- p, q: instantaneous active and reactive power, respectively.
- V_{gd}, V_{gq}: d-axis and q-axis components of the grid-side voltage.
- I_{gd}, I_{gq}: d-axis and q-axis components of the grid-side current.

To obtain the fundamental components of active and reactive power, the instantaneous powers p and q are passed through low-pass filters to remove high-frequency components. The filtered

active and reactive powers are then compared with the reference values ($P_{\text{ref}}, Q_{\text{ref}}$), and Equation 16 uses PI controllers to process these power errors and generate the reference d–q currents.

$$\begin{aligned} I_{\text{ref,d}} &= K_{P,d}\left(P_{\text{ref}} - p\right) + K_{I,d}\int \left(P_{\text{ref}} - p\right) dt \\ I_{\text{ref,q}} &= K_{P,q}\left(Q_{\text{ref}} - q\right) + K_{I,q}\int \left(Q_{\text{ref}} - q\right) dt \end{aligned} \tag{16}$$

Alternatively, the d–q reference currents are obtained from Equation 17, which uses $P_{\text{ref}}, Q_{\text{ref}}$ and the measured voltages ($V_{gd}, V_{gq}, I_{gd}, I_{gq}$).

$$\begin{aligned} I_{\text{ref,d}} &= \frac{2}{3}\frac{P_{\text{ref}}V_{gd} + Q_{\text{ref}}V_{gq}}{V_{gd}^2 + V_{gq}^2} \\ I_{\text{ref,q}} &= \frac{2}{3}\frac{P_{\text{ref}}V_{gq} - Q_{\text{ref}}V_{gd}}{V_{gd}^2 + V_{gq}^2} \end{aligned} \tag{17}$$

Equation 18 uses the PI-based current control loop to generate the voltage references ($V_{\text{ref},d}, V_{\text{ref},q}$) from the measured and reference currents.

$$\begin{aligned} V_{\text{ref,d}} &= K_{P,d2}\left(I_{\text{ref,d}} - I_{gd}\right) + K_{I,d2}\int \left(I_{\text{ref,d}} - I_{gd}\right) dt + V_{gd} - \omega L_f I_{gq} \\ V_{\text{ref,q}} &= K_{P,q2}\left(I_{\text{ref,q}} - I_{gq}\right) + K_{I,q2}\int \left(I_{\text{ref,q}} - I_{gq}\right) dt + V_{gq} + \omega L_f I_{gd} \end{aligned} \tag{18}$$

Where $V_{\text{ref,d}}$ and $V_{\text{ref,q}}$ are the d-axis and q-axis voltage references for the VSC, respectively. The terms $K_{P,d2}$ and $K_{I,d2}$ represent the proportional and integral gains for the d-axis current controller, while $K_{P,q2}$ and $K_{I,q2}$ correspond to the proportional and integral gains for the q-axis current controller. The variable L_f denotes the filter inductance, and ω represents the angular frequency of the grid. Additionally, V_{gd} and V_{gq} are the feed-forward voltages used to decouple the d and q axes.

The feed-forward terms V_{gd} and V_{gq}, along with the cross-coupling terms $\omega L_f I_{gq}$ and $\omega L_f I_{gd}$, are used to decouple the d and q axes and improve the dynamic performance of the control system (Teodorescu, 2011; Yazdani, 2010). The average model of the BESS and wind generator VSC is depicted in Figure 1, adapted from Alghamdi and Cañizares (2021).

2.4.2 Controller design and stability considerations

The controllers are tuned using well-established methodologies, such as those described in Teodorescu (2011); Gole et al. (2005), to optimize the performance of the BESS. The tuning process involves selecting appropriate values for the PI controller gains ($K_{P,d}$, $K_{I,d}$, $K_{P,q}$, $K_{I,q}$, $K_{P,d2}$, $K_{I,d2}$, $K_{P,q2}$, $K_{I,q2}$) to ensure fast and stable tracking of power and current references.

The stability and reliability of the BESS under challenging conditions are further enhanced through careful tuning of the phase-locked loop (PLL), as suggested by Yazdani (2010). This process minimizes the effects of unbalanced and harmonically distorted voltages. Additionally, modal estimation methodologies for worst-case scenarios, based on small-signal analysis (Nasr-Azadani et al., 2014), inform the tuning approach, enhancing the BESS's performance in adverse situations.

2.4.3 Integration into the microgrid

By incorporating this well-designed and properly tuned BESS model operating in grid-feeding mode, the microgrid can effectively manage the variability of renewable energy sources and maintain stable voltage and frequency profiles, even in the presence of rapid power fluctuations.

2.5 Wind generator model

The model for the Type 4 wind generators (WGs) with a voltage source converter (VSC) interface operates similarly to the BESS converter described in Section 2.4. The control strategy for the WG also follows the grid-feeding control mode, where it provides active and reactive power according to reference values. However, unlike the BESS, the wind generator is set to operate at unity power factor, meaning that it provides only active power and does not contribute to reactive power support.

The primary difference from the BESS model is in how the active power reference is determined. In the wind generator model, the active power reference $P_{ref}(t)$ is defined by Equation 19, where $P_{ref}(t) = P_{measured}(t)$ based on actual wind turbine measurements.

$$P_{\text{ref}}(t) = P_{\text{measured}}(t) \tag{19}$$

where $P_{\text{ref}}(t)$ is the active power reference at time t, and $P_{\text{measured}}(t)$ represents the actual measured active power output from the wind turbine at time t, obtained from reference Farrokhabadi et al. (2018), Farrokhabadi et al. (2017).

Since the wind turbine operates at unity power factor, the reactive power reference is set to zero, i.e., $Q_{\text{ref}} = 0$. All other control aspects such as the current reference calculations and internal control loops are identical to those described in detail in Section 2.4.

3 Proposed distributed consensus-based voltage and frequency control

This section introduces a distributed consensus-based VFC strategy for isolated microgrids, extending the work in Nasirian et al. (2016); Alghamdi (2022a). The approach integrates primary and secondary control by regulating DERs' active and reactive power outputs. A specialized voltage control mode is incorporated to manage fault-induced delayed voltage recovery (FIDVR) events, ensuring seamless coordination between active power sharing and frequency regulation.

The key features of the proposed distributed VFC strategy include:

- A voltage control loop that adjusts the voltage setpoints of DERs based on the measured frequency deviations and the estimated global average voltage, ensuring effective frequency regulation and voltage recovery during FIDVR events.
- A reactive power sharing mechanism that utilizes a proximity-based prioritization scheme and a distributed voltage estimator to achieve accurate and efficient sharing of reactive power among DERs, enhancing the microgrid's ability to mitigate voltage sags caused by FIDVR.

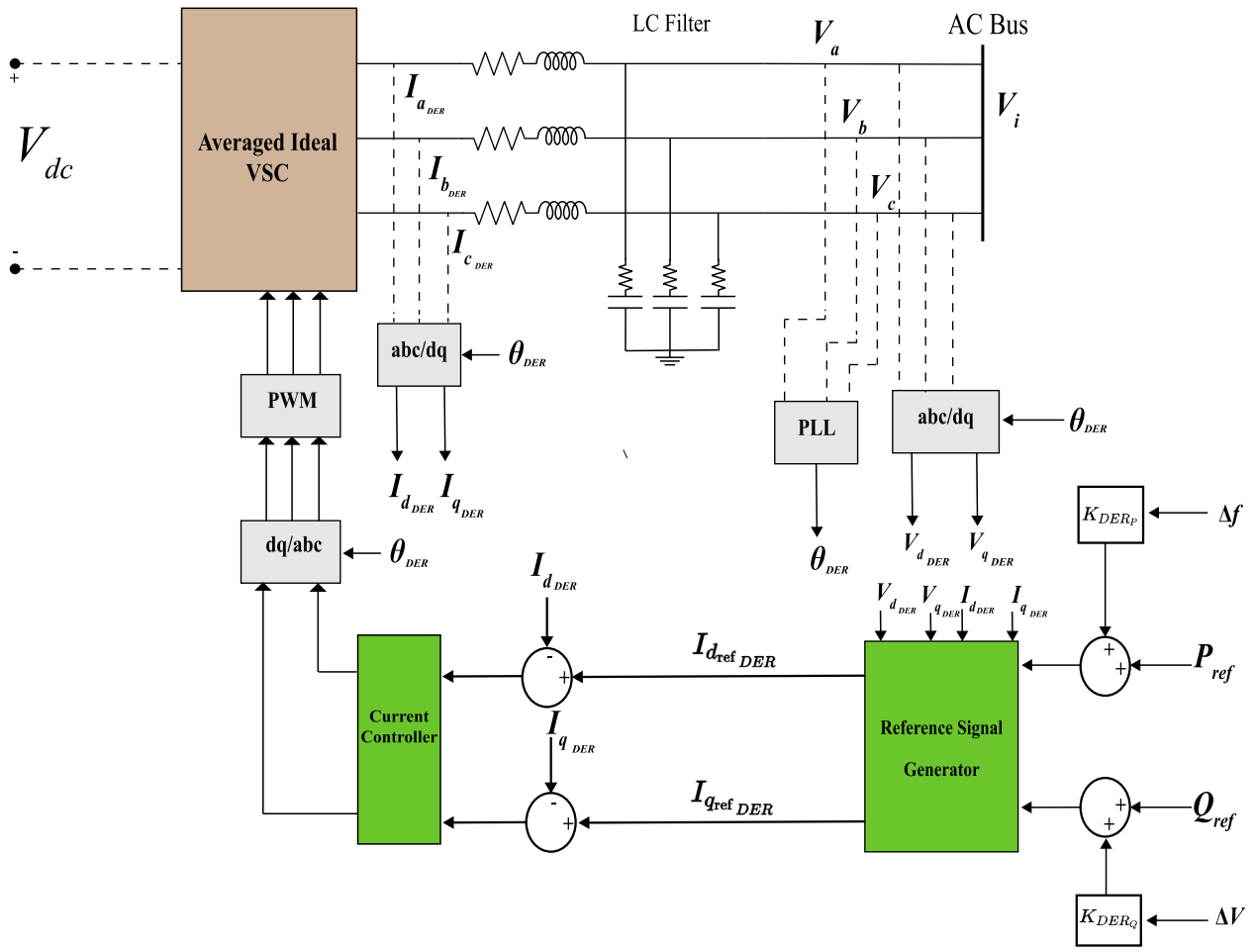

FIGURE 1
BESS and wind generator VSC average model. (Reprinted/adapted with permission from Alghamdi and Cañizares (2021). © 2021 IEEE).

- An active power control loop that coordinates with the VFC to maintain frequency stability and ensure proper active power sharing among DERs, utilizing the reserves created by the VFC.
- Seamless coordination between the VFC and active power control loops through proper tuning of control parameters and the inclusion of a voltage recovery coordination term in the active power setpoint calculation.

The proposed distributed VFC strategy aims to improve the microgrid's performance in terms of frequency regulation, voltage stability, and FIDVR mitigation, while ensuring efficient power sharing among DERs. The following subsections provide a detailed description of the proposed control architecture and its key components.

3.1 Communication graph

The proposed distributed consensus-based VFC scheme relies on a communication graph that enables information exchange among the DERs within the microgrid. The communication graph is represented by $\boldsymbol{G} = (\mathcal{V}, \mathcal{E})$, where $\mathcal{V}$ denotes the set of vertices or nodes corresponding to the DERs, and $\mathcal{E}$ represents the set of edges or communication links between the DERs (Nasirian et al., 2016).

The adjacency matrix $A_G = [a_{ij}]$ is used to describe the connectivity of the communication graph, where $a_{ij} = 1$ if there is a communication link between DER i and DER j, and $a_{ij} = 0$ otherwise. The communication links are assumed to be bidirectional, allowing for the exchange of information between neighboring DERs.

To ensure robustness against communication link failures, the proposed communication architecture employs spanning trees, which maintain graph connectivity even during a single link outage. This approach enhances the reliability and resilience of the distributed VFC scheme, ensuring uninterrupted coordination among the DERs.

The communication graph plays a crucial role in the distributed consensus-based VFC scheme, enabling the exchange of voltage, frequency, and power information among the DERs. This information exchange facilitates the coordination of the DERs' output powers and the implementation of the proposed control algorithms, ultimately leading to improved voltage and frequency regulation, reactive power sharing, and FIDVR mitigation in the microgrid.

TABLE 2 Modified VFC controller actions based on frequency deviation and voltage level.

Condition	Frequency deviation	Voltage level	Controller action
1	Significant	Within limits	$\alpha_f > 1, \alpha_v = 1$
	$(\Delta f > \overline{\Delta f}$ or $\Delta f < \underline{\Delta f})$	$(\underline{V_{MG}} \le \overline{V_i} \le \overline{V_{MG}})$	Increase gains, regulate frequency
2	Significant	Low due to FIDVR	$\alpha_f > 1, \alpha_v = 0$
	$(\Delta f > \overline{\Delta f}$ or $\Delta f < \underline{\Delta f})$	$(\overline{V_i} < \underline{V_{MG}})$	Increase gains, bring voltage to nominal
3	Within limits	Within limits	$\alpha_f = 1, \alpha_v = 1$
	$(\underline{\Delta f} \le \Delta f \le \overline{\Delta f})$	$(\underline{V_{MG}} \le \overline{V_i} \le \overline{V_{MG}})$	Maintain normal controller behavior

3.2 Voltage control loop

The proposed controller coordinates DERs to regulate microgrid frequencies through active power control and VFC, while addressing FIDVR events. It incorporates loops for DER power output regulation, considering voltage-dependent load coupling. A power-sharing mechanism ensures coordination between distributed active power and voltage controllers.

Using an exponential model for microgrid loads, a distributed consensus controller governs frequency by adjusting DER voltage setpoints. To address unequal voltage distribution and improve FIDVR response, the proposed scheme tackles reactive power sharing issues caused by varying DER-to-common point impedances. The distributed control approach is governed by Equations 20, 21. Equation 20 defines V_{VFC} via lead–lag compensation, while Equation 21 combines frequency deviation Δf and voltage feedback $\left(V_{\mathrm{nom}} - \overline{V_i}\right)$ through the gains α_f *and* α_v.

$$V_{VFC} = \beta_{VFC} \frac{\left(1 + \tau_{1_{VFC}} s\right)}{\left(1 + \tau_{2_{VFC}} s\right)} \cdot \left(\alpha_f \cdot K_{P_{VFC}} + \frac{\alpha_f \cdot K_{I_{VFC}}}{s}\right) \cdot \left(\alpha_v \cdot \Delta f + (1 - \alpha_v) \cdot \left(V_{nom} - \overline{V_i}\right)\right) \tag{20, 21}$$

where Δf represents $(f_0 - f_{MG})$, locally measured as defined in Equation 14. β_{VFC}, $K_{P_{VFC}}$, and $K_{I_{VFC}}$ are VFC control parameters, while $\tau_{1_{VFC}}$ and $\tau_{2_{VFC}}$ denote lead-lag time constants. The nominal microgrid voltage is V_{nom}, and $\overline{V_i}$ is node *i*'s estimated global average voltage. Gain adjustment factors based on frequency deviation and voltage level are α_f and α_v, respectively.

The VFC controller adjusts the voltage setpoints of the DERs based on the frequency deviation and voltage level, subject to the following limits:

- Voltage limits: $\underline{V_{MG}} = 0.9$ pu, $\overline{V_{MG}} = 1.1$ pu.
- Frequency limits: $\underline{f_{MG}} = 59.8$ Hz, $\overline{f_{MG}} = 60.2$ Hz.

As shown in Equation 22, V_{VFC} must remain between V_{MG} and $\overline{V}_{MG}$, enforcing the hard voltage limits of the microgrid.

$$\underline{V_{MG}} < V_{VFC} < \overline{V_{MG}} \tag{22}$$

where the microgrid's minimum and maximum tolerable voltages are denoted by $\underline{V_{MG}}$ and $\overline{V_{MG}}$, respectively.

The controller operates based on the frequency deviation and voltage level, as summarized in Table 2. During normal conditions (i.e., when the voltage level is within limits), $\alpha_v = 1$, and the VFC regulates the frequency by adjusting the voltage setpoints based on the frequency deviation Δf. During FIDVR (i.e., when the voltage level is low), $\alpha_v = 0$, and the VFC aims to bring the voltage to the nominal value by adjusting the voltage setpoints based on the voltage error $(V_{nom} - \overline{V_i})$.

The distributed consensus VFC incorporates V_{VFC} as follows:

$$V_i^* = \frac{K_{I_V}}{s}\left(V_{VFC} - \overline{V_i}\right) + \frac{K_{I_Q}}{s}\left(\sum_{i=1}^{n} a_{ij}\left(\frac{Q_{DER_j}}{\beta_{Q_j} \cdot Q'_{DER_j}} - \frac{Q_{DER_i}}{\beta_{Q_i} \cdot Q'_{DER_i}}\right)\right) \quad \forall i \tag{23}$$

where $\overline{V_i}$ represents node *i*'s estimated global average voltage magnitude, obtained from the distributed voltage estimator. K_{I_V} and K_{I_Q} are distributed voltage controller parameters. Local DER *i*'s reference input voltage and output reactive power are denoted by V_i^* and Q_{DER_i}, respectively. Adjacent DER *j*'s output reactive power is Q_{DER_j}. Maximum reactive power capacities for local and adjacent DERs are Q'_{DER_i} and Q'_{DER_j}. The communication system linking DERs determines a_{ij}, as described in Section 3.1. Reactive power support factors based on proximity to the fault location are β_{Q_i} for DER *i* and β_{Q_j} for DER *j*.

In Equation 23, the VFC incorporates two terms: one comparing $\overline{V_i}$ (from the distributed voltage estimator) with the VFC reference voltage, and another for normalized reactive power error to ensure proportional reactive power sharing among DERs. The reactive power regulator compares each DER's local normalized reactive power with its neighbors', considering reactive power support factors (β_{Q_i} and β_{Q_j}) based on proximity to fault location during FIDVR events. This approach allows for adjusting DER reactive power to equalize normalized reactive power across all DERs, while prioritizing support from DERs closer to the fault. Consequently, each DER is loaded according to its rating and fault proximity, enhancing the distributed consensus VFC's effectiveness in mitigating FIDVR. The reactive power support factors (β_{Q_i} and β_{Q_j}) are crucial for prioritizing reactive power contribution based on fault proximity, as detailed in the next subsection.

3.2.1 Proximity-based reactive power support prioritization

To enhance the controller's response to FIDVR events, a proximity-based reactive power support prioritization mechanism is implemented. This mechanism assigns higher reactive power support priority to DERs that are electrically closer to the fault location, enabling them to contribute more effectively to mitigating voltage sags during FIDVR events.

This is achieved by introducing a proximity factor, γ_i, for each DER i, which represents the electrical proximity to the fault location. The proximity factor is calculated based on the voltage sag experienced at each DER during the fault. DERs closer to the fault will experience larger voltage sags.

Calculation of the Proximity Factor γ_i

The proximity factor γ_i is determined through a three-step process:

1. Local Voltage Sag Calculation:

As defined by Equation 24, the local voltage sag ΔV_i is the difference between the nominal voltage V_{nom} and the local voltage measurement V_i at DER node i.

$$\Delta V_i = V_{nom} - V_i \tag{24}$$

where V_{nom} is the nominal voltage magnitude, and V_i is the local voltage measurement at DER node i.

2. Information Sharing and Distributed Max-Consensus Algorithm:

DERs share their local voltage sag measurements with their neighboring DERs according to the communication topology defined by the adjacency matrix A_G. A distributed max-consensus algorithm is then employed to determine the maximum voltage sag experienced across the microgrid. The max-consensus algorithm is iterative, as shown in Equation 25, where $M_i(k+1) = \max\{M_i(k), M_j(k)\}$.

$$M_i(k+1) = \max\left\{M_i(k), M_j(k) \;\; \forall\, j \in N_i\right\} \tag{25}$$

where $M_i(k)$ is the local variable at iteration k, N_i is the set of neighbors of DER i, and $M_i(0) = \Delta V_i$.

Equation 26 shows that $\lim_{k\to\infty} M_i(k) = \max_i \Delta V_i$, indicating convergence to the global maximum voltage sag.

$$\lim_{k\to\infty} M_i(k) = \max_i \Delta V_i \quad \forall i \tag{26}$$

3. Proximity Factor Calculation:

Next, each DER computes its proximity factor γ_i using Equation 27, which normalizes the local voltage sag by the global maximum ΔV_i.

$$\gamma_i = \frac{\Delta V_i}{M_i(\infty)} \tag{27}$$

This ratio provides a normalized measure of how close each DER is to the fault location.

By incorporating the proximity factor into the reactive power sharing mechanism, the controller ensures that DERs closer to the fault contribute more reactive power, which is essential for faster voltage recovery during FIDVR events.

3.2.2 Integration into the voltage control loop

The proximity-based reactive power support prioritization is integrated into the distributed consensus VFC through the reactive power support factors β_{Q_i} in Equation 23. During FIDVR events, DERs with higher β_{Q_i} values (closer to the fault) will adjust their voltage setpoints to inject more reactive power into the microgrid, aiding in voltage recovery.

This approach enhances the effectiveness of the VFC by:

- The distributed control strategy implements a dynamic reactive power support mechanism that intelligently directs resources from DERs positioned to make the most effective contributions to voltage recovery.
- Through coordinated control actions, the system achieves enhanced voltage stability, resulting in accelerated voltage recovery periods and a more robust voltage profile throughout the microgrid network.
- The controller's responsive design actively counteracts FIDVR phenomena by reducing induction motor stalling duration while simultaneously minimizing associated negative impacts on system stability.

The distributed nature of the algorithm ensures scalability and robustness, as each DER only requires local measurements and communication with neighboring DERs.

3.2.3 Distributed voltage estimator

The estimated global average voltage $\overline{V_i}$ is calculated by Equation 28, where $\overline{V_j}$ is each neighbor's estimated average voltage.

$$\overline{V_i} = V_i + \beta_{est}\frac{\left(1+\tau_{1_Q}s\right)}{\left(1+\tau_{2_Q}s\right)}\frac{K_{I_{est}}}{s}\left(\sum_{j\in N_i} a_{ij}\left(\overline{V_j} - \overline{V_i}\right)\right) \quad \forall i \tag{28}$$

where V_i denotes the local voltage measurement at DER node i, and $\overline{V_j}$ is the neighboring node's average microgrid voltage estimate. Estimator parameters are represented by β_{est}, $K_{I_{est}}$, τ_{1_Q}, and τ_{2_Q}.

The distributed voltage estimator not only assists in frequency regulation but also plays a crucial role in the proximity-based reactive power support prioritization by providing accurate voltage information required for calculating the proximity factors.

The detailed discussion on tuning the control parameters, including $\beta_{Q_{max}}$, can be found in Section 4.2.

3.3 Distributed consensus active power coordination with FIDVR consideration

The proposed distributed active power coordination operates in conjunction with the distributed VFC described in Section 3.2. While both controllers use the frequency deviation term $(f_o - f_{MG})$ in their control actions, the coordination between them is achieved through the proper tuning of the control parameters and the introduction of an adaptive gain adjustment mechanism for the active power control loop.

The distributed consensus method for active power coordination is defined by Equations 29, 30, 31, and 32. Equation 29 sets the DER active power reference, while Equations 30 and 31 adapt the control gains under low-voltage conditions.

Finally, Equation 32 coordinates local power flow references among DERs in a distributed manner.

$$P_{DER_{ref_i}} = (f_o - f_{MG})\left(K_P^{adp} + \frac{K_I^{adp}}{s}\right) \forall i \tag{29}$$

$$\text{where } K_P^{adp} = \begin{cases} K_P^{FIDVR}, & \text{if } \overline{V_i} < \underline{V_{MG}} \\ K_P, & \text{otherwise} \end{cases} \tag{30}$$

$$K_I^{adp} = \begin{cases} K_I^{FIDVR}, & \text{if } \overline{V_i} < \underline{V_{MG}} \\ K_I, & \text{otherwise} \end{cases} \tag{31}$$

$$P^*_{DER_i} = \frac{K_{I_P}}{s}\left[\sum_{j\in N_i} a_{ij}\left(\frac{P_{DER_j}}{P'_{DER_j}} - \frac{P_{DER_i}}{P'_{DER_i}}\right) + b_i\left(P_{DER_{ref_i}} - \frac{P_{DER_i}}{P'_{DER_i}}\right)\right] \forall i \tag{32}$$

where $\overline{V_i}$ represents the estimated global average voltage at node i. The distributed active power controller's parameters are denoted by K_P, K_I, K_P^{FIDVR}, K_I^{FIDVR}, and K_{I_P}.

Proper tuning of control parameters ensures coordination between the active power controllers and VFC. The gains of the VFC ($K_{P_{VFC}}$ and $K_{I_{VFC}}$) are set to provide a fast response to frequency deviations, while the gains of the active power controller (K_P and K_I) are set to provide a slower, more sustained response. This allows the VFC to quickly adjust the voltage setpoints to regulate the frequency, while the active power controller gradually adjusts the active power setpoints to maintain frequency stability over a longer period.

However, during FIDVR events, an adaptive gain adjustment mechanism is triggered in the active power control loop to maintain the frequency of the system and counteract the behavior of constant power loads, especially stalled induction motor loads. When the estimated global average voltage ($\overline{V_i}$) falls below the minimum tolerable microgrid voltage ($\underline{V_{MG}}$), the gains of the active power controller are adjusted to K_P^{FIDVR} and K_I^{FIDVR}, which are designed to provide a faster and more aggressive response to frequency deviations caused by the constant power load behavior. This adaptive gain adjustment ensures that the active power control loop prioritizes frequency stability during FIDVR events.

When $\overline{V_i}$ is above $\underline{V_{MG}}$, indicating that the voltage is within the acceptable range, the gains of the active power controller remain at their default values (K_P and K_I), providing a slower and more sustained response to maintain frequency stability under normal operating conditions.

By implementing this adaptive gain adjustment mechanism, the proposed active power control loop effectively coordinates with the VFC loop to maintain frequency stability and counteract the impact of constant power loads during FIDVR events, while also providing a stable and sustained response under normal operating conditions.

In Equation 32, neighboring DERs communicate output active powers to local DER i for inner power control loop use. P_{DER_i} tracks $P_{DER_{ref_i}}$ for DER i, while P_{DER_j} represents adjacent DER j's output active power. Maximum active power capacities for local and adjacent DERs are P'_{DER_i} and P'_{DER_j}. The DER communication system determines a_{ij} (0 or 1), as detailed in Section 3.1. b_i is set to 1 for local $P_{DER_{ref_i}}$ signal inclusion in the DER inner control loop, ensuring P_{DER_i} converges to $P_{DER_{ref_i}}$.

The proposed scheme coordinates distributed VFC and active power control through parameter tuning. This maintains frequency stability during severe disruptions while providing fast regulation. The voltage recovery coordination term enhances FIDVR event support, ensuring a coordinated response within microgrid voltage constraints.

A summarized block diagram of the entire distributed consensus-based voltage and frequency control (VFC) strategy is illustrated in Figure 2, showing how the various loops, estimators, and communications interconnect.

4 Simulation results and discussion

4.1 Microgrid test system

The modified CIGRE benchmark microgrid, which has been widely used in various studies (Farrokhabadi et al., 2018; Farrokhabadi et al., 2017; Solanki et al., 2017; Solanki et al., 2019; Farrokhabadi et al., 2016), was employed to test, validate, and compare the performance of the proposed distributed consensus-based VFC scheme described in Section 3. The microgrid topology, as illustrated in Figure 3, was implemented in PSCAD for time-domain simulations, while MATLAB was used to conduct small-perturbation analysis. Using a 12-core CPU (average 4.8 GHz per core) and 32 GB RAM, the simulations were conducted.

The microgrid system had a total load of approximately 9 MVA, which included a 2 MVA induction motor load and a mix of constant impedance (60%), constant current (30%), and constant power (10%) loads. The static loads were modeled as unbalanced, consistent with the original CIGRE microgrid system (Farrokhabadi et al., 2017; Farrokhabadi et al., 2016). As detailed in Section 2, the system's dynamic models for static loads, induction motor load, and DERs were identical to those in the original CIGRE microgrid. Table 3 summarizes the system characteristics.

The microgrid's Type 4 WGs, modeled according to Farrokhabadi et al. (2018), operated at unity power factor. Feeders were represented as coupled π-sections (Farrokhabadi et al., 2017). Implementing the proposed distributed VFC scheme coordinated dispatchable DERs (DUs and BESS), with a 1 μs communication time delay Kansal and Bose (2012).

The use of the modified CIGRE benchmark microgrid allows for a comprehensive evaluation of the proposed VFC scheme under realistic operating conditions and enables a fair comparison with other control strategies reported in the literature. The diverse mix of DERs, unbalanced loads, and detailed dynamic models provide a suitable platform to assess the performance of the proposed controller in terms of frequency regulation, voltage stability, power sharing, and fault-induced delayed voltage recovery (FIDVR) mitigation.

4.2 Tuning of controller parameters

A genetic algorithm (GA) optimization technique was employed to tune the proposed distributed consensus-based VFC scheme's control parameters. These include $K_{P_{VFC}}$, $K_{I_{VFC}}$, $\tau_{1_{VFC}}$, $\tau_{2_{VFC}}$, β_{VFC}, K_{I_V}, K_{I_Q}, K_P, K_I, K_P^{FIDVR}, K_I^{FIDVR}, K_{I_P}, β_{est}, $K_{I_{est}}$, τ_{1_Q}, and τ_{2_Q}. This approach, recognized for efficiently tuning microgrid controller settings (Bevrani, 2017), aimed to enhance overall

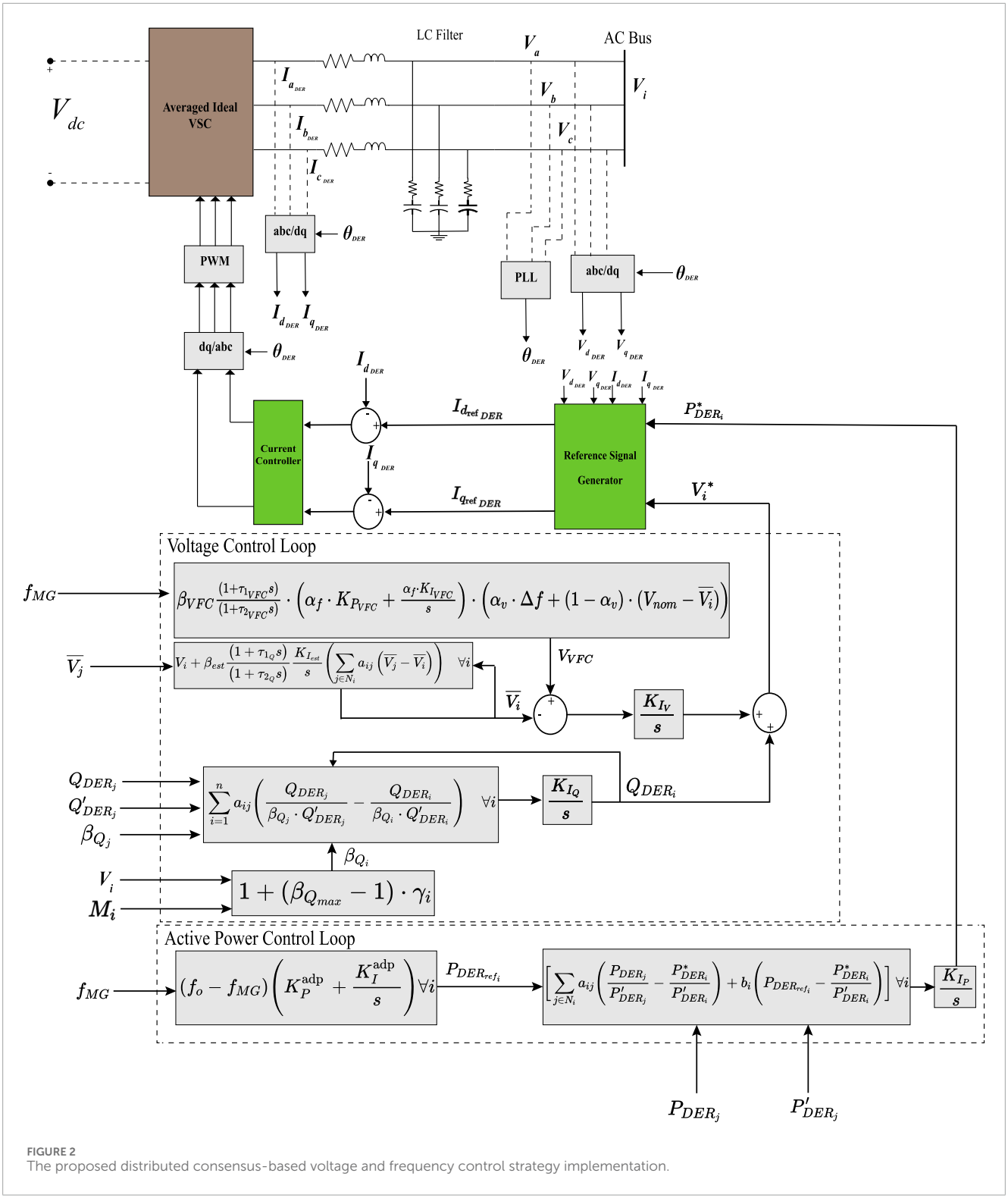

FIGURE 2
The proposed distributed consensus-based voltage and frequency control strategy implementation.

system performance and stability under various conditions. The optimization considered multiple criteria, including minimizing voltage recovery time, ensuring system stability, achieving accurate power sharing, and maintaining frequency stability.

The optimization problem was formulated using a multi-objective function that combines the integral of the time-multiplied absolute value of the error (ITAE) for frequency deviation, voltage deviation, and reactive power sharing error, given by:

$$J = w_1 \int_0^{\infty} t|\Delta f|dt + w_2 \int_0^{\infty} t|\Delta V|dt + w_3 \int_0^{\infty} t|\Delta Q|dt \quad (33)$$

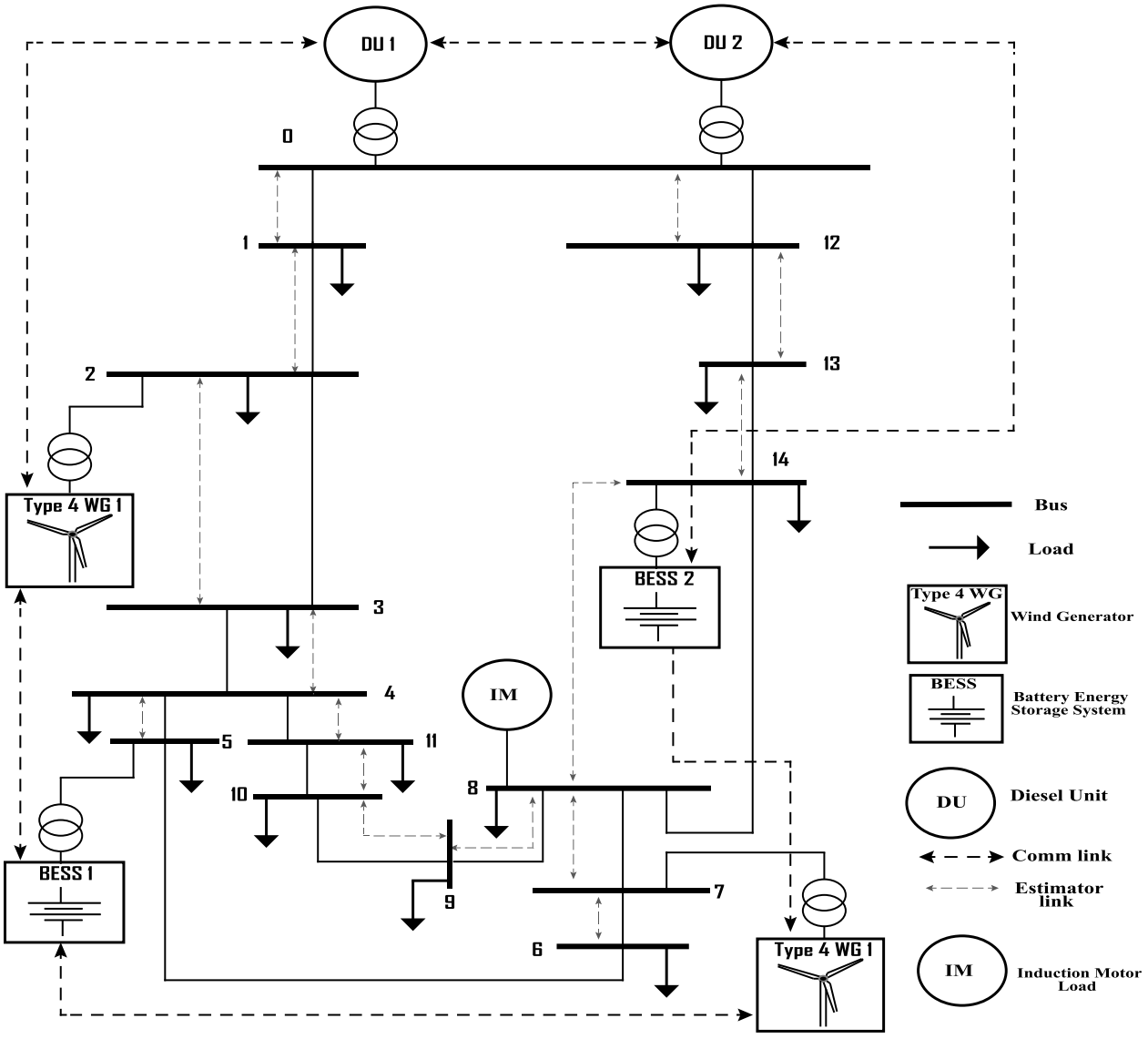

FIGURE 3
CIGRE benchmark microgrid with distributed communication network: modified test system. (Reprinted/adapted with permission from Alghamdi and Cañizares (2021). © 2021 IEEE).

where Δf is the frequency deviation, ΔV is the voltage deviation, ΔQ is the reactive power sharing error, and w_1, w_2, and w_3 are weighting factors that determine the relative importance of frequency stability, voltage stability, and reactive power sharing accuracy in the optimization process. The reactive power sharing error ΔQ is included to ensure that the optimization process considers the effectiveness of the proximity-based reactive power support prioritization mechanism, which is crucial for FIDVR mitigation and overall voltage stability in the proposed VFC strategy.

The genetic algorithm optimization was implemented using PSCAD's built-in GA optimization tool. The process involved the following steps:

- Random generation of an initial population of potential solutions.
- Evaluation of each solution's fitness using the multi-objective function in Equation 33.
- Selection of parent solutions using tournament selection.
- Creation of offspring solutions through simulated binary crossover.
- Application of polynomial mutation to maintain genetic diversity.
- Implementation of elitism to preserve top-performing solutions.
- Termination based on generation count or fitness improvement threshold.

Multiple optimization runs with different random seeds ensured solution robustness. The final control parameters were selected from the best performing solution across all runs.

TABLE 3 Characteristics of the modified CIGRE benchmark Microgrid system used for simulation studies.

Component	Quantity	Rating
Diesel Units (DUs)	2	3 MVA each
Battery Energy Storage Systems (BESS)	4	1 MW each
Wind Generators (WGs) - Type 4	2	1.025 MW each
Induction Motor Load	1	2 MVA
Total Load (including Induction Motor)	-	9 MVA
Load Composition (excluding Induction Motor)	60% constant impedance, 30% constant current, 10% constant power	
Feeders	Modeled as coupled π-sections	

TABLE 4 GA optimization-derived tuned control parameters.

Tuned control parameters			
$K_{P_{VFC}}$	2.3	K_P	1.9
$K_{I_{VFC}}$	8.7	K_I	6.8
$\tau_{1_{VFC}}$	0.14	K_P^{FIDVR}	2.2
$\tau_{2_{VFC}}$	0.18	K_I^{FIDVR}	7.5
β_{VFC}	1.25	K_{I_V}	9.2
β_{est}	1.15	K_{I_Q}	1.3
K_{I_p}		1.1	
$K_{I_{est}}$	5.5	τ_{1_Q}	0.22
τ_{2_Q}	0.3	$\beta_{Q_{max}}$	1.535

To evaluate the controller's performance and determine the optimal parameter values, the microgrid system was subjected to various disturbances, such as load changes, DER outages, fault-induced delayed voltage recovery (FIDVR) events, and communication delays. The GA minimized the objective function Equation 33 until the optimization converged, yielding the tuned controller parameters.

The tuned values of the key control parameters are presented in Table 4. These values were obtained by considering the specific characteristics of the microgrid system, the desired performance criteria, and the results from the GA optimization.

The tuned values of the control parameters ensure that the proposed VFC scheme provides effective frequency regulation, voltage stability, FIDVR mitigation, and accurate reactive power sharing among the DERs. The adaptive gain adjustment mechanism for the active power control loop, with K_P^{FIDVR} and K_I^{FIDVR}, ensures a fast and robust response to frequency deviations caused by the constant power load behavior of stalled induction motors during FIDVR events. The proximity-based reactive power sharing, governed by I_Q and $\beta_{Q_{max}}$, prioritizes the reactive power support from DERs closer to the fault location, enhancing the effectiveness of the distributed consensus VFC in mitigating FIDVR.

The GA optimization approach allows for a systematic and efficient tuning process, considering the complex interactions between the various control loops, the specific requirements of the microgrid system, and the additional challenges posed by communication delays and FIDVR events. The resulting tuned parameters provide a balanced trade-off between the different performance objectives, ensuring the stable and reliable operation of the microgrid under various operating conditions.

4.3 Simulation scenarios

To comprehensively evaluate the performance of the proposed distributed consensus-based VFC strategy, four simulation scenarios were designed to test the microgrid under various operating conditions and disturbances. These scenarios were chosen to demonstrate the capabilities of the proposed controller in regulating frequency, mitigating fault-induced delayed voltage recovery (FIDVR), maintaining stable operation in the presence of communication delays, and handling different fault durations.

Scenario 1: Sudden load increase during low wind power output.

In this introductory scenario, a sudden load increase is applied to the microgrid at t = 105 s, coinciding with the lowest output power from the wind generators. This scenario aims to demonstrate the effectiveness of the proposed VFC strategy in regulating the microgrid frequency and maintaining stable operation under challenging conditions. The performance of the proposed controller is compared to the base case with conventional droop control to highlight its superior frequency regulation capabilities.

Scenario 2: Three-phase fault at Bus 8 causing FIDVR.

To evaluate the proposed VFC strategy's ability to mitigate FIDVR, a three-phase fault is applied to Bus 8 at t = 20 s. This scenario is designed to assess the impact of FIDVR on the microgrid voltage and compare the voltage recovery performance of the proposed controller with the base case and conventional VFC strategies. By demonstrating improved voltage recovery, this scenario showcases the effectiveness of the proposed VFC strategy in enhancing the microgrid's resilience to FIDVR events.

Scenario 3: Three-phase fault at Bus 8 with communication delays.

Building upon Scenario 2, this scenario introduces communication delays to the microgrid system while a three-phase fault is applied at Bus 8. The purpose of this scenario is to investigate the robustness of the proposed VFC strategy in the presence of communication delays, which can potentially impact the performance of distributed control schemes. By evaluating the controller's performance under these conditions, this scenario demonstrates the resilience and practicality of the proposed VFC strategy in real-world microgrid applications.

Scenario 4: Impact of fault duration on voltage recovery.

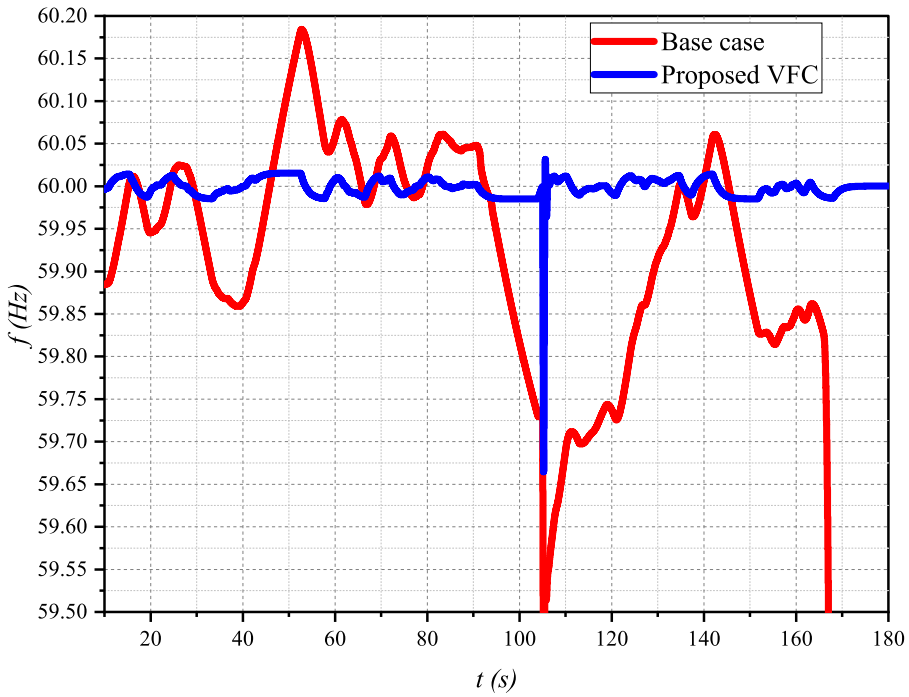

FIGURE 4
Frequency response of the microgrid system under the proposed VFC strategy and the base case with conventional droop control, subjected to a sudden load increase at t = 105 s.

In this scenario, the impact of fault duration on the voltage recovery time is investigated for both the proposed VFC strategy and the conventional VFC. A three-phase fault is applied at Bus 8 with varying durations, specifically 0.045s and 0.05s. The purpose of this scenario is to assess the effectiveness of the proposed VFC strategy in handling different fault durations and to compare its performance with the conventional VFC in terms of voltage recovery time and stability. By demonstrating faster voltage recovery times and improved stability under different fault durations, this scenario highlights the robustness and superiority of the proposed VFC strategy in mitigating FIDVR events and maintaining microgrid stability.

These four simulation scenarios provide a comprehensive evaluation of the proposed VFC strategy's performance under various operating conditions, disturbances, and challenges. By assessing the controller's effectiveness in regulating frequency, mitigating FIDVR, maintaining stable operation in the presence of communication delays, and handling different fault durations, these scenarios demonstrate the versatility, resilience, and practicality of the proposed VFC strategy in real-world microgrid applications.

4.4 Performance evaluation of the proposed VFC strategy

The performance of the proposed distributed consensus-based VFC strategy was evaluated under a challenging scenario where the microgrid experiences a sudden load increase at t = 105 s, coinciding with the lowest output power from the wind generators. Figure 4 shows the frequency response of the microgrid system under the proposed VFC strategy (blue line) compared to the base case with conventional droop control (red line).

In the base case, the microgrid frequency drops significantly, reaching a minimum of approximately 59.55 Hz, and undergoes several oscillations before slowly recovering and eventually collapses again. In contrast, the proposed VFC strategy demonstrates superior performance, with a less severe frequency drop (minimum of around 59.85 Hz), faster and smoother recovery, and fewer oscillations.

The improved frequency response under the proposed VFC strategy is attributed to the distributed consensus-based control architecture, the coordination between the VFC and active power control loops, and the optimally tuned control parameters. These results highlight the effectiveness of the proposed VFC strategy in maintaining microgrid frequency stability and ensuring smooth operation under challenging scenarios.

In the following subsections, we will further investigate the performance of the proposed VFC strategy under different simulation scenarios, including fault-induced delayed voltage recovery (FIDVR) events, and compare its performance with existing control methods reported in the literature.

Scenario 2: Three-phase fault at Bus 8 causing FIDVR.

To evaluate the performance of the proposed VFC strategy in mitigating fault-induced delayed voltage recovery (FIDVR), a three-phase fault was applied at Bus 8 at t = 20 s, lasting for 0.045 s. The voltage response of the microgrid was observed, focusing on the average microgrid voltage (Figure 5) and the voltage at the terminal of the induction motor load (Figure 6).

In the base case with conventional VFC (red line), the average microgrid voltage (Figure 5) experiences a severe drop to

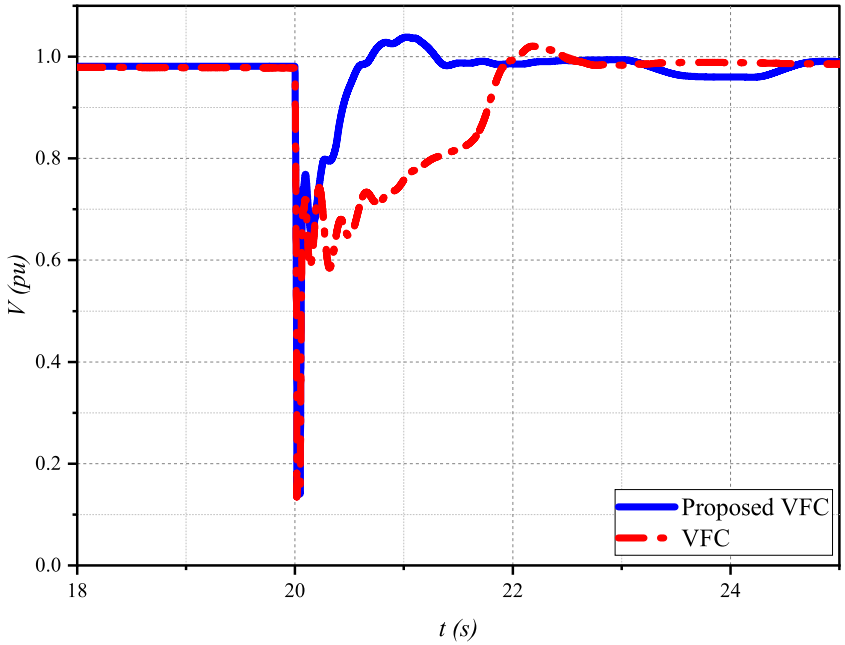

FIGURE 5
Average microgrid voltage during a three-phase fault at Bus 8, comparing the proposed VFC strategy with conventional VFC.

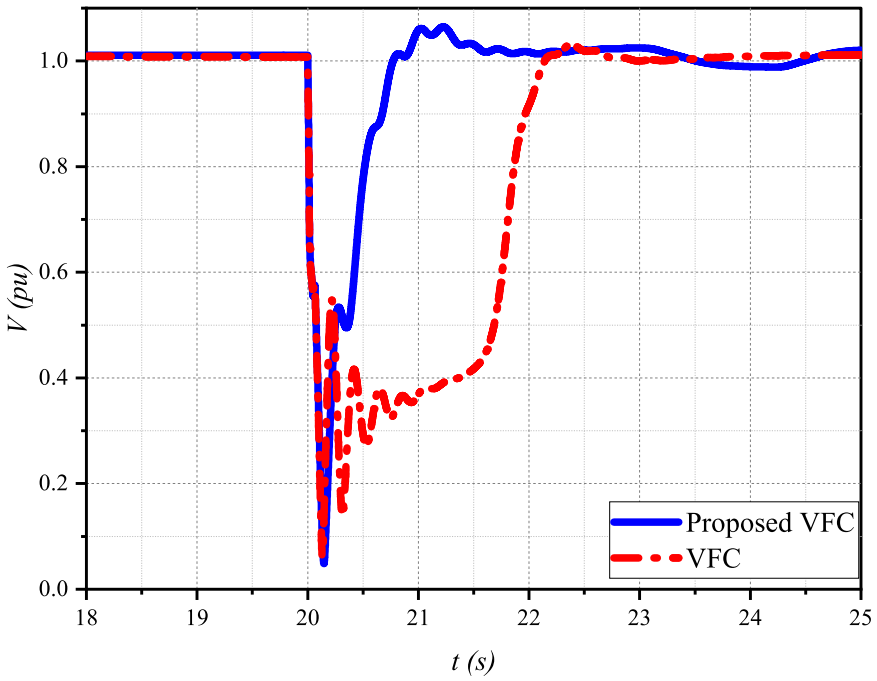

FIGURE 6
Induction motor terminal voltage during a three-phase fault at Bus 8, comparing the proposed VFC strategy with conventional VFC.

approximately 0.1 pu during the fault. After the fault is cleared, the voltage recovers slowly, taking more than 2 s to reach the pre-fault level. This delayed voltage recovery is primarily caused by the stalling of induction motor loads, which draw a large amount of reactive power during the post-fault period.

Similarly, the voltage at the induction motor terminal (Figure 6) drops to nearly zero during the fault and exhibits a delayed recovery in the base case. The motor voltage remains below 0.8 pu for more than 2 s after the fault is cleared, indicating a prolonged stalling condition.

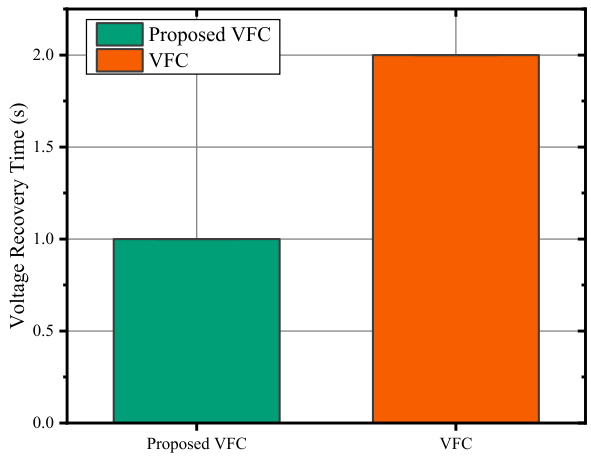

FIGURE 7
Comparison of voltage recovery time between the proposed VFC strategy and the conventional VFC.

In contrast, the proposed VFC strategy (blue line) demonstrates a significantly improved voltage recovery performance. The average microgrid voltage (Figure 5) drops to approximately 0.1 pu during the fault. However, after the fault is cleared, the voltage recovers much faster, reaching the pre-fault level within 1 s. This rapid voltage recovery is achieved by the proposed VFC's ability to detect the FIDVR condition and adjust the voltage setpoints of the DERs to provide additional reactive power support.

The voltage at the induction motor terminal (Figure 6) also exhibits a faster recovery under the proposed VFC strategy. The motor voltage reaches 0.8 pu within 1 s after the fault is cleared, indicating a shorter stalling duration and improved motor performance.

Figure 7 compares the voltage recovery time of the proposed VFC strategy and the conventional VFC. The proposed VFC demonstrates a significantly faster voltage recovery, taking approximately 0.5 s, while the conventional VFC requires around 2 s to restore the voltage to its nominal value. This highlights the superior performance of the proposed VFC strategy in mitigating FIDVR and ensuring rapid voltage recovery.

The superior voltage recovery performance of the proposed VFC strategy can be attributed to several factors:

1. The modified VFC equation Equation 21, which includes a voltage error term and a switching mechanism based on the estimated global average voltage, enables the controller to prioritize voltage recovery during FIDVR events.
2. The proximity-based reactive power support prioritization ensures that DERs closer to the fault location provide more reactive power support, effectively mitigating the voltage sags caused by FIDVR.
3. The distributed voltage estimator provides an accurate representation of the microgrid voltage profile, allowing for a coordinated and targeted response to FIDVR events.

These results demonstrate the effectiveness of the proposed VFC strategy in mitigating FIDVR and ensuring a faster and more stable voltage recovery compared to conventional VFC methods. By maintaining higher voltage levels during faults and reducing the duration of induction motor stalling, the proposed VFC strategy enhances the microgrid's resilience to disturbances and improves overall system stability.

In Scenario 2, the reactive power sharing performance of the proposed VFC strategy was evaluated during a three-phase fault at Bus 8, which caused a fault-induced delayed voltage recovery (FIDVR) event. Figure 8 shows the reactive power output of BESS 1 and BESS 3 during the post-fault period.

The reactive power sharing mechanism in the proposed VFC strategy is based on the proximity of each DER to the fault location, as described in the power sharing Equation 23. After the fault is cleared, BESS 3, which is closer to the fault location at Bus 8, provides a higher reactive power output compared to BESS 1. This is in accordance with the proximity-based reactive power sharing mechanism, where DERs closer to the fault location are assigned higher reactive power support factors (β_{Q_i}) and, consequently, contribute more to the voltage recovery process.

The gradual reduction in reactive power output of both BESS units after the fault is cleared indicates the effectiveness of the proposed VFC strategy in mitigating the FIDVR event and restoring the microgrid voltage to its nominal value. The proximity-based reactive power sharing ensures that the DERs closer to the fault location bear a larger share of the reactive power burden, thereby minimizing the overall voltage deviations and enhancing the speed of voltage recovery.

These results demonstrate the successful implementation of the proximity-based reactive power sharing mechanism in the proposed VFC strategy, which prioritizes the contribution of DERs closer to the fault location during FIDVR events. By effectively coordinating the reactive power support provided by the DERs, the proposed VFC strategy ensures a faster and more stable voltage recovery, enhancing the microgrid's resilience to disturbances.

Figure 9 shows the speed of the induction motor load connected to the microgrid during Scenario 2. The motor speed experiences a sudden drop due to the voltage sag caused by the three-phase fault at Bus 8. In the case of conventional VFC (red line), the motor speed drops to approximately 0.92 pu and takes a long time to recover after the fault is cleared, indicating the impact of fault-induced delayed voltage recovery (FIDVR) on the motor's performance.

In contrast, the proposed VFC strategy (blue line) demonstrates a significantly improved motor speed response. Although the motor speed drops during the fault, it recovers much faster after the fault is cleared compared to the conventional VFC case. The faster recovery of the motor speed under the proposed VFC strategy can be attributed to the improved voltage recovery performance, as discussed in the previous sections.

The proposed VFC strategy demonstrates superior performance in restoring the system frequency and voltage to nominal values compared to the conventional VFC approach, as evident from Figures 1, 2.

Figure 10 shows that the active power output of BESS 1 and 3 using the proposed VFC strategy exhibits a more rapid and coordinated response to the fault-induced disturbance compared to BESS 1 using conventional VFC. The proposed VFC enables the

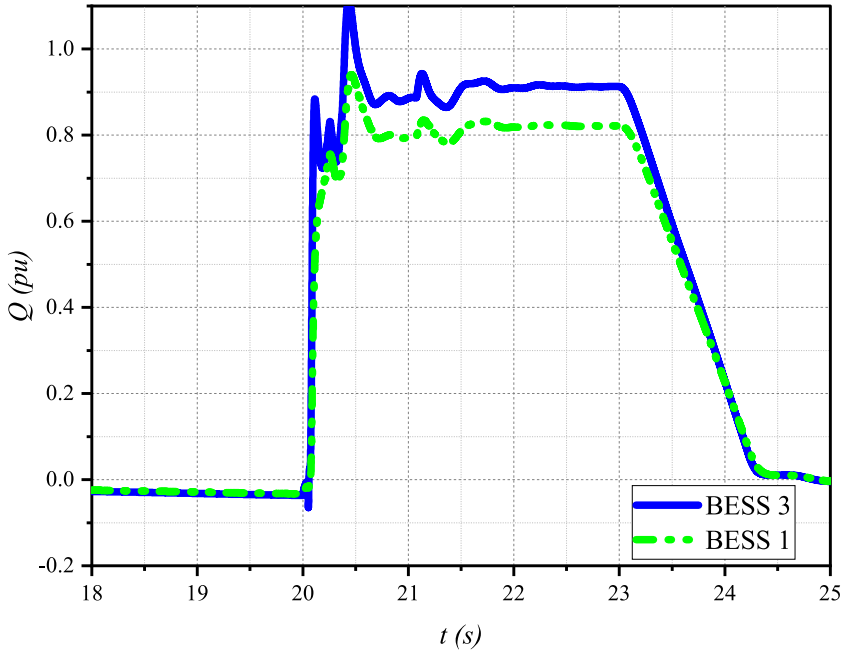

FIGURE 8
Reactive power output of BESS 1 and BESS 3 during the post-fault period, demonstrating the proximity-based reactive power sharing mechanism of the proposed VFC strategy.

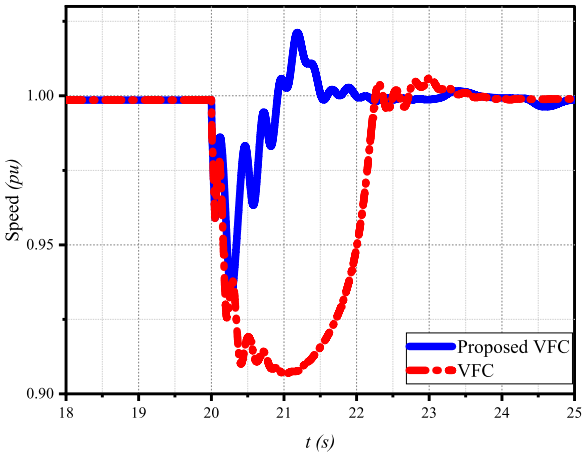

FIGURE 9
Induction motor speed during and after a three-phase fault at Bus 8, comparing the proposed VFC strategy with conventional VFC.

BESS units to quickly inject active power into the system to support frequency recovery.

Figure 11 illustrates the system frequency response under both the proposed and conventional VFC strategies. The proposed VFC achieves a faster frequency recovery, with the frequency returning to its nominal value within approximately 2 s after the fault. In contrast, the conventional VFC exhibits a slower and more oscillatory frequency response, taking longer to stabilize.

The effectiveness of the proposed VFC strategy can be attributed to the adaptive gain adjustment mechanism implemented in the active power control loop. During the FIDVR event, the gains of the active power controller are dynamically adjusted to provide a faster and more aggressive response to frequency deviations caused by the constant power load behavior of stalled induction motor loads. This adaptive approach ensures that the active power control loop prioritizes frequency stability, enabling a more rapid and robust frequency recovery.

The coordinated action of the BESS units, facilitated by the distributed consensus control architecture, further enhances the overall system performance. The BESS units collectively contribute to frequency regulation and voltage support, leading to a more stable and resilient microgrid operation.

Scenario 3: Three-phase fault at Bus 8 with communication delays.

The impact of communication delays on the performance of the proposed VFC strategy was evaluated by applying a three-phase fault at Bus 8 and observing the average microgrid voltage recovery under different time delay conditions (150 μs, 50 m, 100 m, and 500 m), as shown in Figure 12.

The results demonstrate that the proposed VFC strategy can restore the average microgrid voltage to its nominal value, even in the presence of communication delays. However, the voltage recovery time increases with larger time delays. In the worst-case scenario (500 m delay), the voltage recovery is significantly slower, taking approximately 1.5 s to reach the nominal value after the fault is cleared. Despite the slower recovery, no instability is observed, highlighting the robustness of the proposed VFC strategy.

The slower voltage recovery with larger time delays is attributed to the delayed communication and coordination among the DERs. Nevertheless, the proposed VFC strategy's

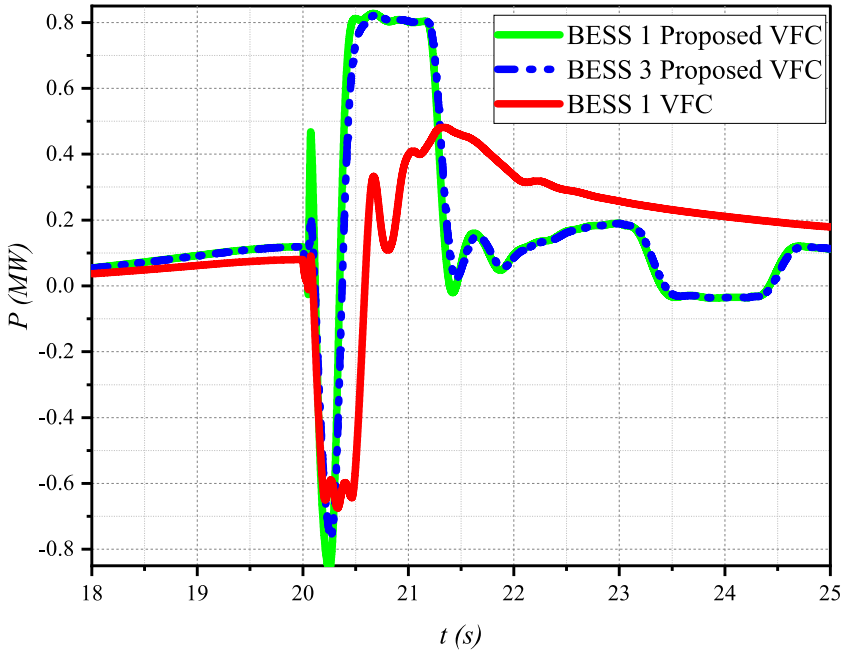

FIGURE 10
Active power output of BESS units under the proposed VFC and conventional VFC strategies.

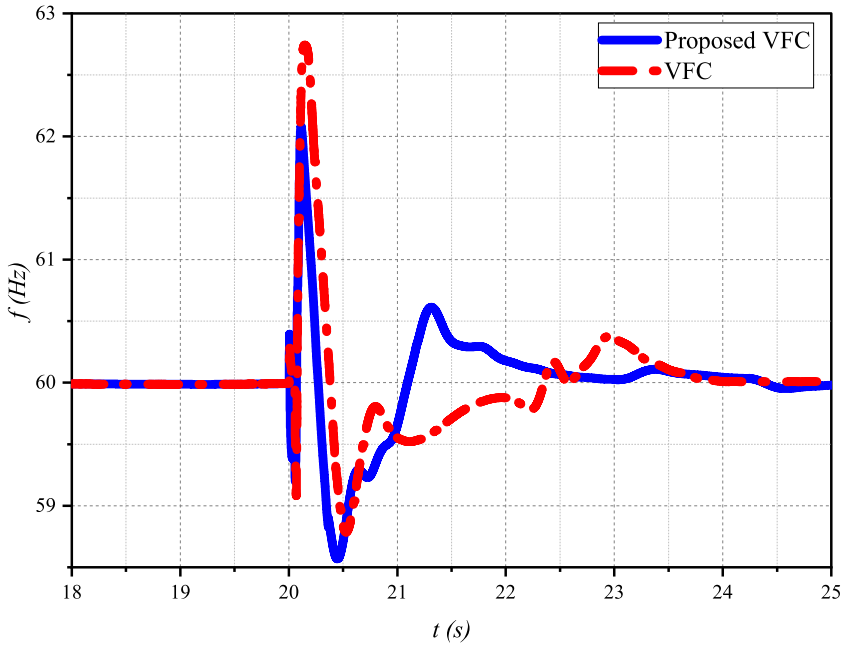

FIGURE 11
System frequency response under the proposed VFC and conventional VFC strategies.

adaptive gain adjustment mechanism and the coordination between the VFC and active power control loops help maintain stability and eventually restore the voltage to its nominal value.

These results demonstrate the resilience and effectiveness of the proposed VFC strategy in handling communication delays, ensuring reliable operation of the microgrid under realistic conditions where communication infrastructure may introduce latencies.

Scenario 4: Impact of fault duration on voltage recovery.

Figure 13 shows the voltage at the terminal of the induction motor (IM) load for fault durations of 0.045s and 0.05s, comparing the proposed VFC and the conventional VFC.

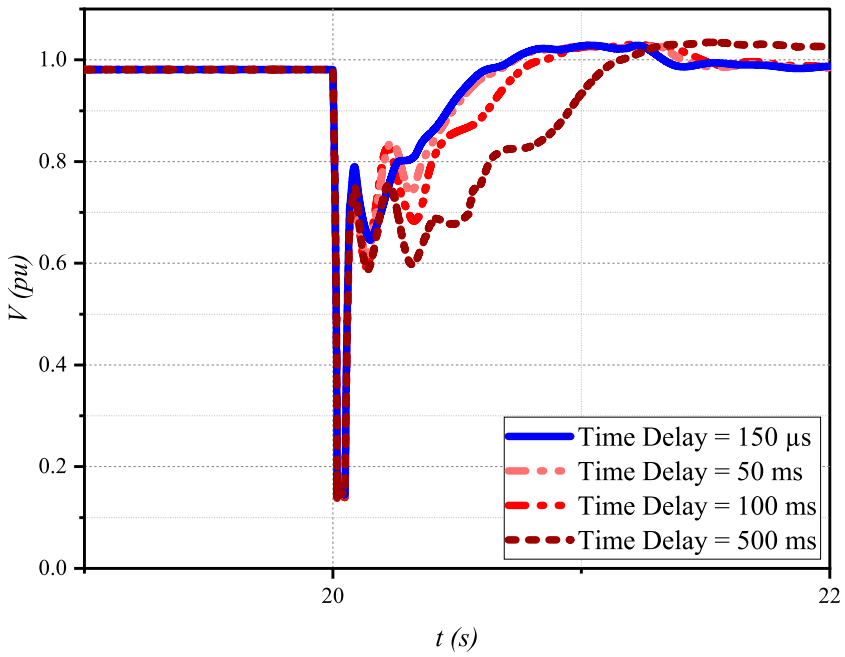

FIGURE 12
Average microgrid voltage recovery under different communication delay conditions.

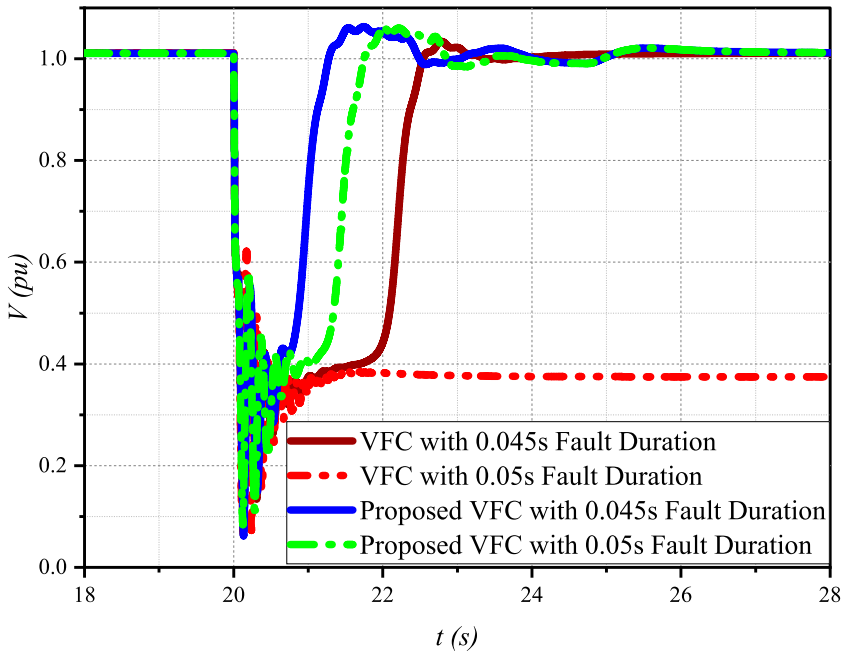

FIGURE 13
Induction motor load voltage recovery comparison between the proposed VFC and conventional VFC for fault durations of 0.045s and 0.05s.

The proposed VFC achieves faster voltage recovery compared to the conventional VFC for both fault durations. With a fault duration of 0.05s, the conventional VFC fails to recover the voltage, and the IM load stalls, while the proposed VFC restores the voltage within approximately 1 s after the fault is cleared. For a fault duration of 0.045s, the proposed VFC exhibits a faster voltage recovery than the conventional VFC. Longer fault durations lead to slower voltage recovery for both control strategies.

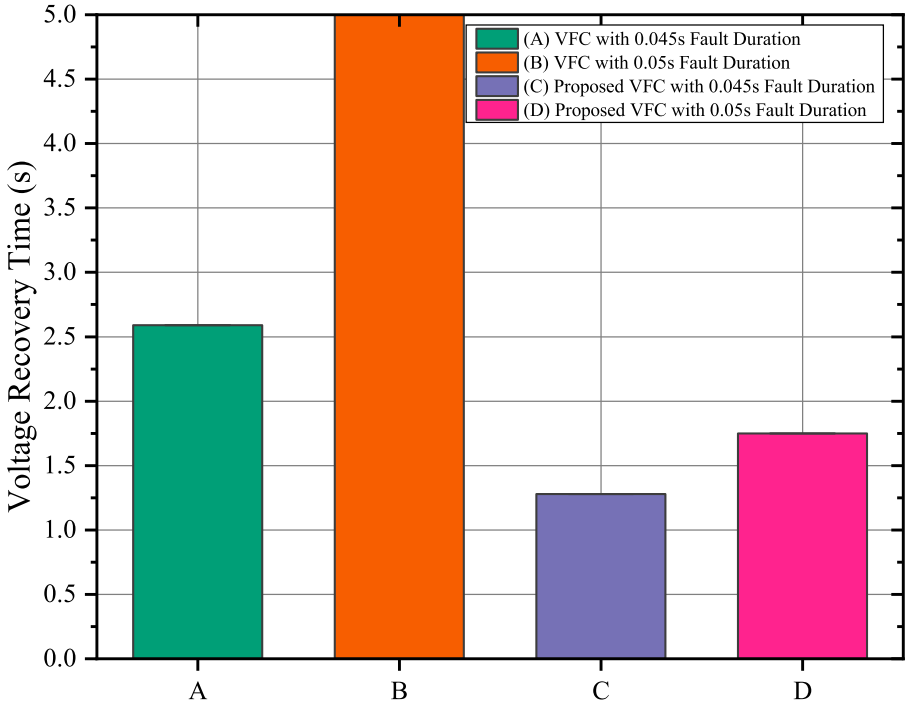

FIGURE 14
Comparison of voltage recovery times for the proposed VFC and conventional VFC under different fault durations.

TABLE 5 Summary of performance metrics comparing proposed VFC and conventional methods.

Performance metric	Conventional VFC	Proposed VFC	Improvement
Voltage Recovery Time (0.045s Fault)	2.5 s	1.1 s	56% reduction
Voltage Recovery Time (0.05s Fault)	Failure to recover	1.3 s	Successful recovery
Frequency Deviation under Load Increase	±0.45 Hz	±0.15 Hz	66% reduction
Maximum Communication Delay Tolerated	N/A	500 m	-
Reactive Power Sharing Error	High	Low	Improved sharing

Figure 14 compares the voltage recovery time of the proposed VFC strategy and the conventional VFC for different fault durations. The proposed VFC consistently achieves faster voltage recovery times compared to the conventional VFC, with recovery times of approximately 1.1 s and 1.3 s for fault durations of 0.045s and 0.05s, respectively. In contrast, the conventional VFC exhibits significantly slower recovery times of around 2.5 s for a fault duration of 0.045s and fails to recover the voltage for a fault duration of 0.05s, indicating potential voltage instability.

4.5 Summary of performance improvements

To provide a consolidated overview of the improvements achieved by the proposed VFC strategy, Table 5 presents a comparison of key performance metrics between the proposed VFC and conventional methods.

As observed from Table 5, the proposed VFC strategy reduced the voltage recovery time after a 0.045s fault from 2.5 s to 1.1 s, representing a 56% improvement. Similarly, under sudden load increases, the frequency deviation was limited to ±0.15 Hz with the proposed VFC, compared to ±0.45 Hz with conventional droop control, resulting in a 66% reduction. The table also highlights the controller's robustness to communication delays of up to 500 m and improved reactive power sharing among DERs.

5 Conclusion

This paper presents a novel distributed consensus-based voltage and frequency control (VFC) strategy for isolated microgrids with distributed energy resources (DERs) to regulate frequency and

voltage while effectively mitigating fault-induced delayed voltage recovery (FIDVR) events caused by induction motor load stalling.

The proposed VFC strategy incorporates several innovative features, including a voltage control loop with proximity-based reactive power sharing, an adaptive gain adjustment mechanism in the active power control loop, and a distributed voltage estimator. These components work in concert to ensure effective coordination among DERs during normal operation and FIDVR events.

The inclusion of an adaptive gain adjustment mechanism in the active power control loop allows the controller to dynamically adapt to varying disturbance conditions by adjusting the control gains based on the system's voltage level. During FIDVR events, when the voltage is significantly depressed, the adaptive mechanism increases the control gains, enabling a faster and more aggressive response to frequency deviations caused by the constant power behavior of stalled induction motors. This enhances system robustness by ensuring faster frequency stabilization and improved coordination between voltage and frequency control during disturbances.

Comprehensive simulation results demonstrate the superior performance of the proposed VFC strategy compared to conventional methods. Key achievements include:

- Faster voltage recovery times during FIDVR events—The proposed VFC strategy reduced voltage recovery times by up to 56%, restoring voltage to nominal levels within 1.1 s for a 0.045s fault. In contrast, conventional VFC required 2.5 s (see Figure 14; Table 5).
- Enhanced frequency stability under various operating conditions—During sudden load increases, the proposed VFC limited frequency deviations to within ±0.15 Hz, offering a 66% improvement over the ±0.45 Hz deviations observed with conventional droop control (refer to Figure 4).
- Improved reactive power sharing among DERs—A proximity-based reactive power support prioritization ensured that DERs contributed reactive power in accordance with their proximity to the fault. This approach provided more effective voltage support and balanced reactive power outputs (as shown in Figure 8).
- Robust performance in the presence of communication delays—The proposed VFC maintained stable operation, successfully restoring voltage levels even with communication delays of up to 500 m. This demonstrates robustness that is suitable for real-world scenarios with non-ideal communication infrastructures (illustrated in Figure 12).
- Effective handling of different fault durations—The controller adapted to varying fault durations and successfully recovered voltage levels even when conventional methods failed to do so (see Figure 13), thus enhancing microgrid resilience to disturbances.

These findings confirm that the proposed VFC strategy significantly enhances microgrid performance in terms of voltage recovery, frequency stability, reactive power sharing, and robustness to communication delays and fault conditions.

The implications of this work for future research and practical applications in microgrid control are significant. This study contributes to the development of advanced distributed control strategies capable of addressing complex phenomena in microgrids with high penetration of induction motor loads. The proposed VFC strategy offers a practical solution for improving the resilience and stability of isolated microgrids, particularly in scenarios where network conditions may be less than ideal.

In the broader context of renewable energy integration, this work advances the development of more reliable and stable microgrid systems, which is crucial for increasing the penetration of distributed energy resources in power systems. Future work could focus on experimental validation and real-world implementation to provide further insights into practical challenges and opportunities.

In conclusion, the distributed consensus-based VFC strategy presented in this paper represents a significant advancement in microgrid control techniques. By effectively addressing the challenges of frequency regulation, voltage stability, and FIDVR mitigation through mechanisms such as adaptive gain adjustment in the active power control loop, this work contributes to the ongoing development of more resilient, efficient, and sustainable power systems.

Data availability statement

The original contributions presented in this study are included in the article. Further inquiries can be directed to the corresponding author.

Author contributions

BA: Conceptualization, Data curation, Formal Analysis, Funding acquisition, Investigation, Methodology, Project administration, Resources, Software, Supervision, Validation, Visualization, Writing–original draft, Writing–review and editing.

Funding

The author declares that financial support was received for the research, authorship, and/or publication of this article. This Project was funded by the Deanship of Scientific Research (DSR) at King Abdulaziz University, Jeddah, under grant no. (GPIP: 149-135-2024). The author, therefore, acknowledge with thanks DSR for technical and financial support.

Acknowledgments

The author used OpenAI's GPT-4o model (accessed via the OpenAI API) and Grammarly for language editing and proofreading. These tools were employed solely to improve clarity and grammar; the author takes full responsibility for all final content and conclusions.

Conflict of interest

The author declares that the research was conducted in the absence of any commercial or financial relationships that could be construed as a potential conflict of interest.

Publisher's note

References

Alghamdi, B. (2022a). Distributed voltage frequency control of isolated microgrids. *IEEE Access* 10, 134799–134810. doi:10.1109/ACCESS.2022.3232725

Alghamdi, B. (2022b). Fuzzy logic–based decentralized voltage–frequency control and inertia control of a vsg-based isolated microgrid system. *Energies* 15, 8401. doi:10.3390/en15228401

Alghamdi, B., and Cañizares, C. A. (2021). Frequency regulation in isolated microgrids through optimal droop gain and voltage control. *IEEE Trans. Smart Grid* 12, 988–998. doi:10.1109/TSG.2020.3028472

Benali, A., Khiat, M., Allaoui, T., and Denai, M. (2018). Power quality improvement and low voltage ride through capability in hybrid wind-pv farms grid-connected using dynamic voltage restorer. *IEEE Access* 6, 68634–68648. doi:10.1109/ACCESS.2018.2878493

Bevrani, H. (2017). *Microgrid dynamics and control*. Hoboken, NJ: John Wiley and Sons, Inc.

Bidram, A. (2017). *Cooperative synchronization in distributed microgrid control*. Cham, Switzerland: Springer.

Chapman, S. J. (2011). *Electric machinery fundamentals*. 5th edn. McGraw-Hill Education.

Choi, J., Habibi, S. I., and Bidram, A. (2022). Distributed finite-time event-triggered frequency and voltage control of ac microgrids. *IEEE Trans. Power Syst.* 37, 1979–1994. doi:10.1109/TPWRS.2021.3110263

Farrokhabadi, M., Cañizares, C., and Bhattacharya, K. (2016). "A voltage-based frequency controller for inverter-based systems in microgrids," in *2016 IEEE power and energy society general meeting (PESGM)*, 1–5. doi:10.1109/PESGM.2016.7741281

Farrokhabadi, M., Cañizares, C. A., and Bhattacharya, K. (2017). Frequency control in isolated/islanded microgrids through voltage regulation. *IEEE Trans. Smart Grid* 8, 1185–1194. doi:10.1109/TSG.2015.2479576

Farrokhabadi, M., König, S., Cañizares, C. A., Bhattacharya, K., and Leibfried, T. (2018). Battery energy storage system models for microgrid stability analysis and dynamic simulation. *IEEE Trans. Power Syst.* 33, 2301–2312. doi:10.1109/TPWRS.2017.2740163

Farrokhabadi, M., Simpson-Porco, J. W., and Cañizares, C. A. (2021). "Optimal design of voltage-frequency controllers for microgrids," in *2021 IEEE Madrid PowerTech*, 1–6. doi:10.1109/PowerTech46648.2021.9495073

Gole, A. M., Filizadeh, S., Menzies, R. W., and Wilson, P. L. (2005). Optimization-enabled electromagnetic transient simulation. *IEEE Trans. Power Deliv.* 20, 512–518. doi:10.1109/TPWRD.2004.835385

Gu, W., Tan, Y., Chen, H., and Zhang, X. (2022). Transient stability analysis of induction motor-load system considering the effect of voltage sag. *IEEE Access* 10, 4120–4130. doi:10.1109/ACCESS.2022.3140012

Hossain, M. A., Pota, H. R., Hossain, M. J., and Blaabjerg, F. (2019). Evolution of microgrids with converter-interfaced generations: challenges and opportunities. *Int. J. Electr. Power Energy Syst.* 109, 160–186. doi:10.1016/j.ijepes.2019.01.038

Huang, S., Xiong, L., Zhou, Y., Liu, J., Jia, Q., Li, P., et al. (2023). Distributed predefined-time secondary frequency and average voltage control for islanded ac microgrids. *IEEE Trans. Power Syst.* 38, 4191–4205. doi:10.1109/TPWRS.2022.3209981

Kansal, P., and Bose, A. (2012). Bandwidth and latency requirements for smart transmission grid applications. *IEEE Trans. Smart Grid* 3, 1344–1352. doi:10.1109/TSG.2012.2197229

Krause, P. C., Wasynczuk, O., Sudhoff, S. D., and Pekarek, S. D. (2013). *Analysis of electric machinery and drive systems*. 3 edn. Wiley-IEEE Press.

Ling, C., Hu, J., Liu, J., Yu, T., and Huang, L. (2021). Transient stability analysis of induction motor-load system considering stator flux dynamics. *IEEE Trans. Power Syst.* 36, 4502–4511. doi:10.1109/TPWRS.2021.3057536

Mohiuddin, S. M., and Qi, J. (2022). Optimal distributed control of ac microgrids with coordinated voltage regulation and reactive power sharing. *IEEE Trans. Smart Grid* 13, 1789–1800. doi:10.1109/TSG.2022.3147446

Nasirian, V., Shafiee, Q., Guerrero, J. M., Lewis, F. L., and Davoudi, A. (2016). Droop-free distributed control for ac microgrids. *IEEE Trans. Power Electron.* 31, 1600–1617. doi:10.1109/TPEL.2015.2414457

Nasr-Azadani, E., Cañizares, C. A., Olivares, D. E., and Bhattacharya, K. (2014). Stability analysis of unbalanced distribution systems with synchronous machine and DFIG based distributed generators. *IEEE Trans. Smart Grid* 5, 2326–2338. doi:10.1109/tsg.2014.2321709

Nayeripour, M., Mahboubi-Moghaddam, E., and Aghamohammadi, M. R. (2018). Dynamic state estimation based protection scheme for microgrids with induction motor loads. *IEEE Trans. Smart Grid* 9, 5873–5882. doi:10.1109/TSG.2017.2711022

Olivares, D. E., Mehrizi-Sani, A., Etemadi, A. H., Cañizares, C. A., Iravani, R., Kazerani, M., et al. (2014). Trends in microgrid control. *IEEE Trans. Smart Grid* 5, 1905–1919. doi:10.1109/TSG.2013.2295514

Paredes, L. A., Molina, M. G., and Serrano, B. R. (2023). Enhancing dynamic voltage stability in resilient microgrids using facts devices. *IEEE Access* 11, 66150–66176. doi:10.1109/ACCESS.2023.3291009

Park, B., and Olama, M. M. (2021). A model-free voltage control approach to mitigate motor stalling and fidvr for smart grids. *IEEE Trans. Smart Grid* 12, 67–78. doi:10.1109/TSG.2020.3012308

Solanki, B. V., Bhattacharya, K., and Cañizares, C. A. (2017). A sustainable energy management system for isolated microgrids. *IEEE Trans. Sustain. Energy* 8, 1507–1517. doi:10.1109/TSTE.2017.2692754

Solanki, B. V., Cañizares, C. A., and Bhattacharya, K. (2019). Practical energy management systems for isolated microgrids. *IEEE Trans. Smart Grid* 10, 4762–4775. doi:10.1109/TSG.2018.2868130

Stefopoulos and Meliopoulos (2006). "Induction motor load dynamics: impact on voltage recovery phenomena," in *2005/2006 IEEE/PES transmission and distribution conference and exhibition*, 752–759. doi:10.1109/TDC.2006.1668591

Teodorescu, R. (2011). *Grid converters for photovoltaic and wind power systems*. Piscataway, New Jersey Chichester, West Sussex: IEEE Wiley.

Vandoorn, T. L., Renders, B., Degroote, L., Meersman, B., and Vandevelde, L. (2011). Active load control in islanded microgrids based on the grid voltage. *IEEE Trans. Smart Grid* 2, 139–151. doi:10.1109/TSG.2010.2090911

Wang, W., and de León, F. (2020). Quantitative evaluation of der smart inverters for the mitigation of fidvr in distribution systems. *IEEE Trans. Power Deliv.* 35, 420–429. doi:10.1109/TPWRD.2019.2929547

Wound rotor induction machine (2023). Wound rotor induction machine. Available at: https://www.pscad.com/webhelp/Master_Library_Models/Machines/Wound_Rotor_Induction_Machine/Wound_Rotor_Induction_Machine.htm (Accessed February 11, 2023).

Xu, Y., Sun, H., Gu, W., Xu, Y., and Li, Z. (2019). Optimal distributed control for secondary frequency and voltage regulation in an islanded microgrid. *IEEE Trans. Industrial Inf.* 15, 225–235. doi:10.1109/TII.2018.2795584

Yazdani, A. (2010). *Voltage-sourced converters in power systems: modeling, control, and applications*. Hoboken, N.J: IEEE Press/John Wiley.

Yeager, K. E., and Willis, J. R. (1993). Modeling of emergency diesel generators in an 800 megawatt nuclear power plant. *IEEE Trans. Energy Convers.* 8, 433–441. doi:10.1109/60.257056